Lithosphere–asthenosphere interaction beneath the western United States from the joint inversion of body-wave traveltimes and surface-wave phase velocities

Mathias Obrebski,[1] Richard M Allen,[1] Fred Pollitz[2] and Shu-Huei Hung[3]

[1]*Seismological Laboratory, University of California, Berkeley, CA* 94720, *USA. E-mail: obrebski@berkeley.edu*
[2]*US Geological Survey,* 508 *National Center,* 12201 *Sunrise Valley Drive, Reston, VA,* 20192, *USA*
[3]*National Taiwan University, Taipei,* 106, *Taiwan*

SUMMARY

The relation between the complex geological history of the western margin of the North American plate and the processes in the mantle is still not fully documented and understood. Several pre-USArray local seismic studies showed how the characteristics of key geological features such as the Colorado Plateau and the Yellowstone Snake River Plains are linked to their deep mantle structure. Recent body-wave models based on the deployment of the high density, large aperture USArray have provided far more details on the mantle structure while surface-wave tomography (ballistic waves and noise correlations) informs us on the shallow structure. Here we combine constraints from these two data sets to image and study the link between the geology of the western United States, the shallow structure of the Earth and the convective processes in mantle. Our multiphase DNA10-S model provides new constraints on the extent of the Archean lithosphere imaged as a large, deeply rooted fast body that encompasses the stable Great Plains and a large portion of the Northern and Central Rocky Mountains. Widespread slow anomalies are found in the lower crust and upper mantle, suggesting that low-density rocks isostatically sustain part of the high topography of the western United States. The Yellowstone anomaly is imaged as a large slow body rising from the lower mantle, intruding the overlying lithosphere and controlling locally the seismicity and the topography. The large E–W extent of the USArray used in this study allows imaging the 'slab graveyard', a sequence of Farallon fragments aligned with the currently subducting Juan de Fuca Slab, north of the Mendocino Triple Junction. The lithospheric root of the Colorado Plateau has apparently been weakened and partly removed through dripping. The distribution of the slower regions around the Colorado Plateau and other rigid blocks follows closely the trend of Cenozoic volcanic fields and ancient lithospheric sutures, suggesting that the later exert a control on the locus of magmato-tectonic activity today. The DNA velocity models are available for download and slicing at http://dna.berkeley.edu.

Key words: Inverse theory; Body waves; Surface waves and free oscillations; Seismic tomography; Dynamics of lithosphere and mantle; North America.

INTRODUCTION

The western margin of the North American plate is marked by the active region located mainly on accreted and composite terrains west of the Rocky Mountains Front, which contrasts with the stable and autochthonous cratonic region to the east (Fig. 1). The subduction of the Farallon plate that started ∼150 Ma has been shaping the Pacific Northwest and modifying its crust and upper mantle. Its remnant, the Juan de Fuca-Gorda slab is still subducting beneath Cascadia. The flattening of the Farallon slot and its contact with the North American lithosphere (Livacarri & Perry 1981; Dumitru *et al.* 1991; van Hunen *et al.* 2002; English *et al.* 2003; Saleeby 2003;

DeCelles 2004; O'Driscoll *et al.* 2009) is thought to have controlled the intense phase of crustal shortening, uplift and lithosphere modification (metasomatism) during the Sevier-Laramide orogenies (140–45 Ma). Post-Laramide volcano-tectonic activity is controlled by the removal of the Farallon slab and includes westward propagating arc-like volcanism (the 'ignimbrite flare-up'), wide spread uplift all over the western United States and gravitational collapse in the Rio Grande Rift and Basin and Range. Neogene to Quaternary volcanic activity is also marked by the outpouring of the Columbia River Basalts (CRB) ∼17 Ma and the enigmatic time-progressive sequences of silicic centres in the Yellowstone-Snake River Plains (YSRP) and the High Lava Plains (HLP) (Morgan 1971; Pierce &

GJI Seismology
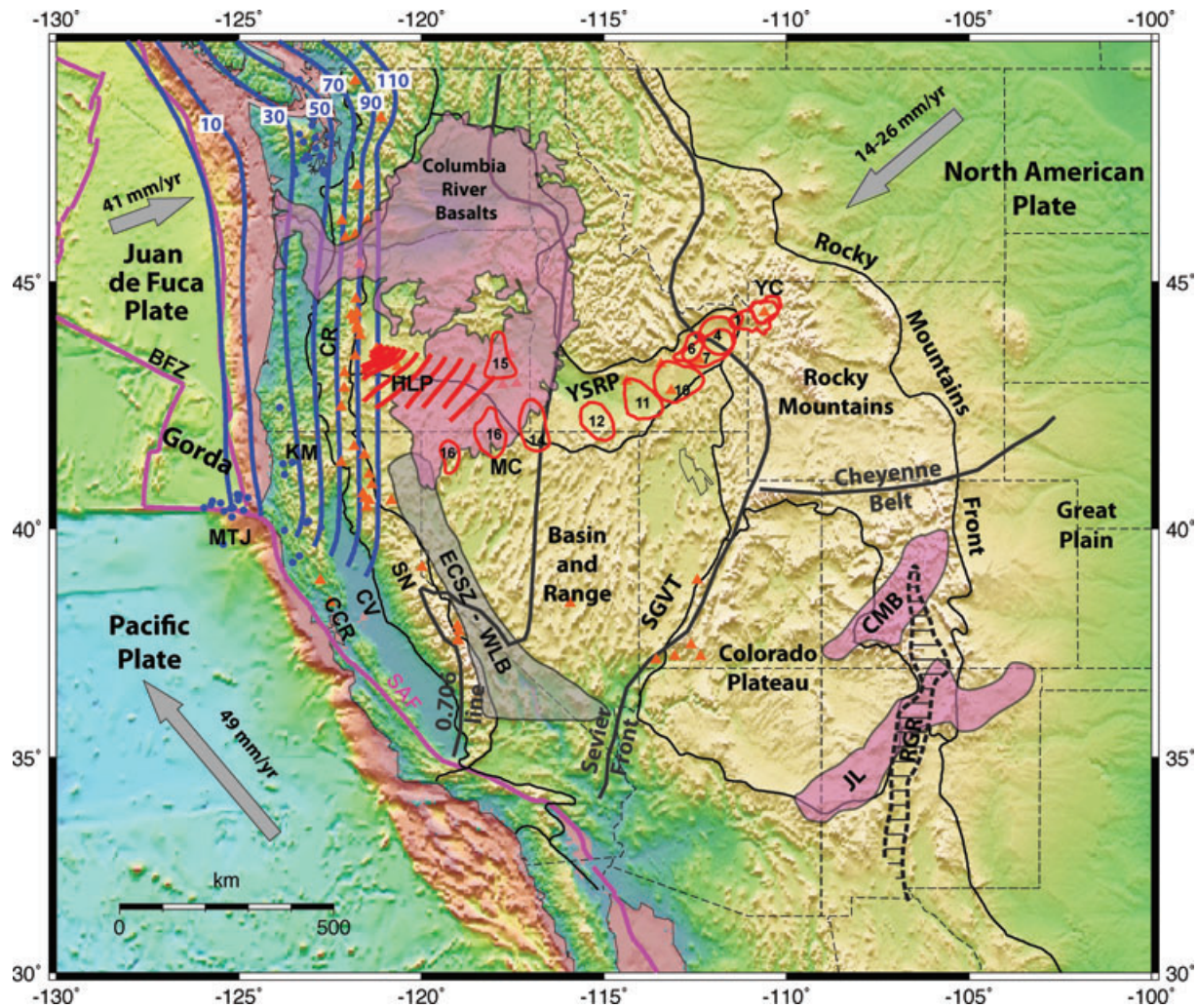
Figure 1. Geological-tectonic features of the western United States overlaid on topography. North from the Mendocino Triple Junction (MTJ), the Gorda and Juan de Fuca (JdF) plates are subducting beneath the North American plate with an oblique convergence rate of (on average) 41 mm yr^{-1}. The estimated depth of the top of subducting slab is shown with blue contours labelled in km (McCrory *et al.* 2006). The location of all $M > 4$ earthquakes with depth ≥ 35 km since 1970 are shown as blue dots. Volcanoes are shown as orange triangles. The Yellowstone Hotspot Track exhibits a series of time-progressive calderas (red outline) from McDermitt Caldera (MC) to the currently active Yellowstone Caldera (YC). The track is approximately parallel to the absolute plate motion of North America, which is estimated to be 14–26 mm yr^{-1} to the southwest. Numbers indicate the age of the calderas (in Ma). The Columbia River Flood Basalt Province was a massive outpouring of basalt from ∼16.6 to ∼15.0 Ma and is shown in pink. The Laramide Colorado Mineral Belt (CMB) and late Miocene to present Jemez Lineament (JL) are also shown is pink. The grey lines show major structural and compositional boundaries. The Cheyenne Belt separates Archean basement to the north from Proterozoic basement to the south. The 0.706 line is the estimated limit between autochthonous terranes to the east and accreted intraoceanic arcs based on Sr isotopic ratios. The Sevier Front is also close to the miogeocline hingeline. The black striped area is the slightly extended Rio Grande Rift. Other acronyms: BFZ, Blanco Fracture Zone; CCR, California Coastal Range; CR, Cascadia Range; CV, Central Valley; ECSZ-WLB, East California Shear Zone-Walker Lane Belt; HLP, High Lava Plain; KM, Klamath Mountains; SAF, San Andreas Fault; SGVT, Saint George Volcanic Trend; SN, Sierra Nevada; YSRP, Yellowstone-Snake River Plain.

Morgan 1992; Smith & Braile 1994; Dickinson 1997; Humphreys *et al.* 2000; Pierce *et al.* 2000; Christiansen *et al.* 2002; Camp & Ross 2004; Smith *et al.* 2009; Obrebski *et al.* 2010).

The scientific interest generated by the currently active and ancient volcano-tectonic features of the western margin of the North American plate has motivated numerous tomographic studies at the scale of the United States (van der Lee & Nolet 1997; Henstock *et al.* 1998) or with a focus on key features such as the Colorado Plateau (Lee & Grand 1996; Sine *et al.* 2008), the Southern Sierra Nevada Drip (Zandt *et al.* 2004) and the Yellowstone hot-spot track (Yuan & Dueker 2005; Waite *et al.* 2006; Smith *et al.* 2009). The deployment of the Earthscope USArray network with its ∼70 km station spacing has been providing high quality seismic data which

has been used to illuminate with high resolution the structure of the mantle beneath the United States using body-waves (Burdick *et al.* 2008; Roth *et al.* 2008; Sigloch *et al.* 2008; Tian *et al.* 2009; Obrebski *et al.* 2010, Schmandt & Humphreys 2010).

Nevertheless, with typically ∼70 km station spacing, the USArray-based body-wave models do not have sufficient vertical resolution to map the velocity anomalies located in the shallow lithosphere, which is an issue for the study of the lithosphere–asthenosphere interaction. The simultaneous inversion of constraints from body- and surface-waves allows combination of the complementary properties of these two data sets (Masters *et al.* 1996; Mégnin & Romanowicz 2000; Schmid *et al.* 2008). In particular, the addition of constraints from short period surface-waves

to a body-wave model can theoretically provide resolution in the shallowest part of the joint model, where the body-waves lose resolution (West *et al.* 2004). Here we present our regional multiphase shear-wave velocity model for the western United States obtained using an approach different to previous efforts. We jointly invert body-waves traveltime measurements that are an updated version of the data set used by Obrebski *et al.* (2010) and the surface-wave phase velocity observations used in the model of Pollitz & Snoke (2010), to obtained a multiphase tomographic shear-wave velocity model with good resolution from the surface down into the lower mantle. Our model illuminates the link between the surface geology, the shallow structure of the lithosphere and the convection in the sublithospheric mantle.

DATA

The station distribution that we used in this study covers all the major magmato-tectonic features of the active western United States plus the westernmost part of the stable cratonic United States (Fig. 2). Data were recorded from 2006 January to 2010 January. The resulting total area spanned by our model is bounded by the Canadian and Mexican borders, and extends from the Pacific coast to ~100°W including North and South Dakota, Nebraska, Kansas, Oklaoma and Texas. The seismic data used in this study were recorded by the Earthscope Transportable Array, two Earthscope Flexible Array deployments (FACES and Mendocino), the Global Seismograph Network (IRIS/IDA and IRIS/USGS), the Canadian National Seismograph Network (CNSN), GEOSCOPE (GEO), the United States National Seismic Network (USNSN), the ANZA Regional Network (ANZA), the Berkeley Digital Seismograph Network (BDSN), the Cascade Chain Volcano Monitoring Network (CC), the Montana Regional Seismic Network (MRSN), the Northern California Seismic Network (NCSN), the Western Great Basin/Eastern Sierra Nevada Network (WGB/ESN), the Southern California Seismic Network, the University of Oregon Regional Network (UO), the University of Utah Regional Network (UURN), the Pacific Northwest Regional Seismic Network (PNSN), the Yellowstone Wyoming Seismic Network (YWSN) and the Wallowa Network.

Our body-wave data set contains high-quality shear arrivals. Special attention was paid to select only the highest quality data. Our initial data set consisted of events with epicentral distances greater than 30° and magnitudes greater or equal to 5.5. After visual inspection, half of these events were discarded. Arrivals were picked manually as part of the waveform-by-waveform quality control and to provide a marker for the cross correlation that followed. The resulting data set consists of relative traveltime delays (VanDecar & Crosson 1990). Only cross-correlograms in the 0.02–0.1 Hz frequency band where found to have sufficiently high signal-to-noise ratio. Only arrivals that produce a mean correlation coefficient larger or equal to 0.9 are used in the inversion, reducing the total number of data by another ~50 per cent. Our final body-wave shear arrival data set includes 40 053 *S*-wave traveltime measurements from 162 events. Fig. 3 shows a map of the events providing body-wave observations and illustrates that we use a sampling that is as homogeneous as possible.

The surface-wave data set is an updated version of that used by Pollitz & Snoke (2010). We employ 63 281 seismograms generated by 167 teleseismic events of magnitude ≥6.3 and depth <50 km. Complex amplitude spectra of the fundamental-mode Rayleigh waves are obtained at selected periods by means of a three-step
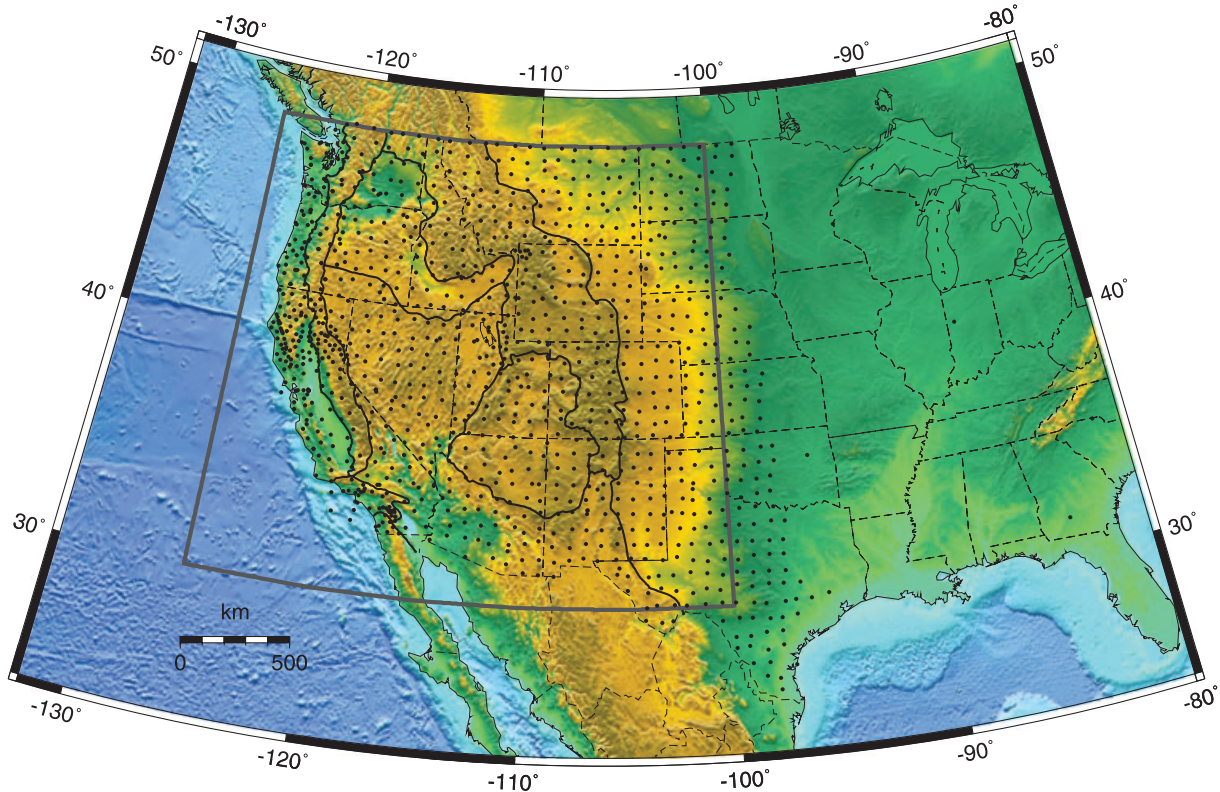
Figure 2. Station distribution overlaid on topography and physiographic boundaries. We used over a thousand stations. The box represents the region with high resolution presented in this manuscript. This map also emphasizes the contrast between the flat, low topography cratonic area and the uplifted, sharp-relief active western United States.
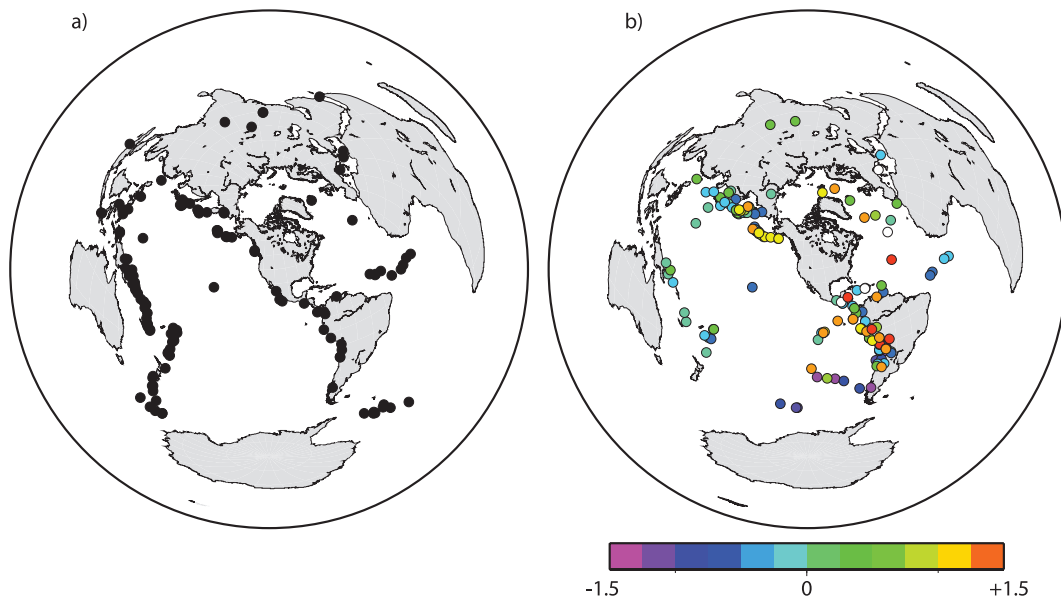
Figure 3. Event distribution. Left and right plots show the events that provided surface-waves and teleseisimic shear-wave arrivals, respectively. On the right plot, the colour scale indicates the amplitude of the event correction terms.

process. First, for each vertical-component seismogram, a spectrogram is constructed using a moving-window taper designed for the period being considered. Second, complex amplitude spectra are obtained at the group-velocity peaks corresponding to the fundamental mode. Third, quality criteria are applied based on the consistency of the group-velocity peaks as a function of period, resulting in a large edited data set. This data set provides constraints on velocity structure from the crust down to the upper mantle. The phase velocities used in this study were measured at 13 periods (125, 100, 83, 67, 59, 50, 40, 33, 27, 25, 22, 20 and 18 s). The sensitivity of the shortest period spans the crust and peaks at 20 km, and the longest period has a broad sensitivity kernel roughly centred on 200 km (see fig. A2 of Pollitz & Snoke 2010).

METHOD

Tomographic images of the Earth's interior are typically obtained from body-waves or surface-waves used separately. Body-waves, which have intrinsically shorter usable wavelengths than surface-waves, provide comparatively good lateral resolution. When the array used for the study has large aperture, which is the case for USArray, regional body-wave tomography also allows imaging of the velocity structure to significant depth, beyond the transition zone. The main limitation of body-wave tomography is the lack of resolution where ray paths do not cross each other, that is, at shallow lithospheric depth. In contrast, surface-wave tomography based on fundamental mode observations is not sensitive to the structure bellow ~300 km. Nevertheless, when short periods surface-waves are included in the inversion, the resulting model has good constraints on the crustal structure. These complementary properties of the body- and surface-waves in terms of depth sensitivity are combined in this study.

Surface-wave relative phase velocities

Following the methodology of Pollitz & Snoke (2010), phase velocity maps are derived by modelling the surface wavefield recorded by

each event as a solution of the 2-D wave equation (Helmholtz equation) on a spherical membrane with laterally varying phase velocity. At a given period, this equation is valid in the presence of smooth structural perturbations (Tromp & Dahlen 1993; Friederich *et al.* 2000), and it is further applicable to the case of relatively rough lateral variations (those which change on the scale of one propagating wavelength) provided that the seismic network is dense enough to account for the interference of multiple plane waves arriving from different directions (Friederich *et al.* 2000). In an approach related to '2-plane' and multiplane wave tomography (Friederich & Wielandt 1995; Forsyth *et al.* 1998; Pollitz 1999; Forsyth & Li 2005; Yang & Forsyth 2006; Yang & Ritzwoller 2008), following Pollitz & Snoke (2010) we account for interfering plane waves and local phase velocity structure simultaneously by parametrizing each observed wavefield as a weighted sum of the 'HG' solutions of Friederich & Wielandt (1995), which implicitly depend upon the local phase velocity. Using observations restricted essentially to a subset of USArray stations about a given locality, we solve simultaneously for the sets of event-HG (2-D-Hermite-Gaussian) weighting coefficients plus the local phase velocity using a grid search. This method is simpler than conventional multiplane-wave tomography and, by taking advantage of the large number of events observed by local arrays of stations, results in robust estimates of phase velocity over the entire area spanned by the TA. Typical error in phase velocity measurements at all periods is about 0.02–0.05 km s^{-1} (see fig. 8 of Pollitz & Snoke 2010). The lateral resolution is approximately equal to the Gaussian weighting distance used to restrict the observations contributing to phase velocity estimation at a given locality, which is about 50 km (eq. 12 of Pollitz & Snoke 2010).

The phase velocity anomalies that are used in the inversion are obtained from the absolute phase velocities by subtracting the phase velocities calculated for a background model. The background model is the western US (WUS) reference model of fig. 17 of Pollitz (2008) with 35 km crustal thickness. To take into account the variation in the crust thickness across the station array, the crustal thickness of the background model was varied. To test the robustness of this correction, we used two different crust models, one based on *P*-to-*S* converted phases (Miller & Levander 2009) and

the other derived from a large number of active experiments across the western United States (Chulick & Mooney 2002). The resulting models are very similar and show only slight differences at crustal depths (Fig. 4). For the remainder of this paper we will focus on and show the model that uses the crust model of Chulick & Mooney (2002).

Body-wave relative traveltimes

In this study we invert the body-wave traveltime data set with a tomographic technique utilizing finite-frequency sensitivity kernels. The banana-doughnut-shaped kernels account for the frequency- and depth-dependent width of the region to which teleseismic
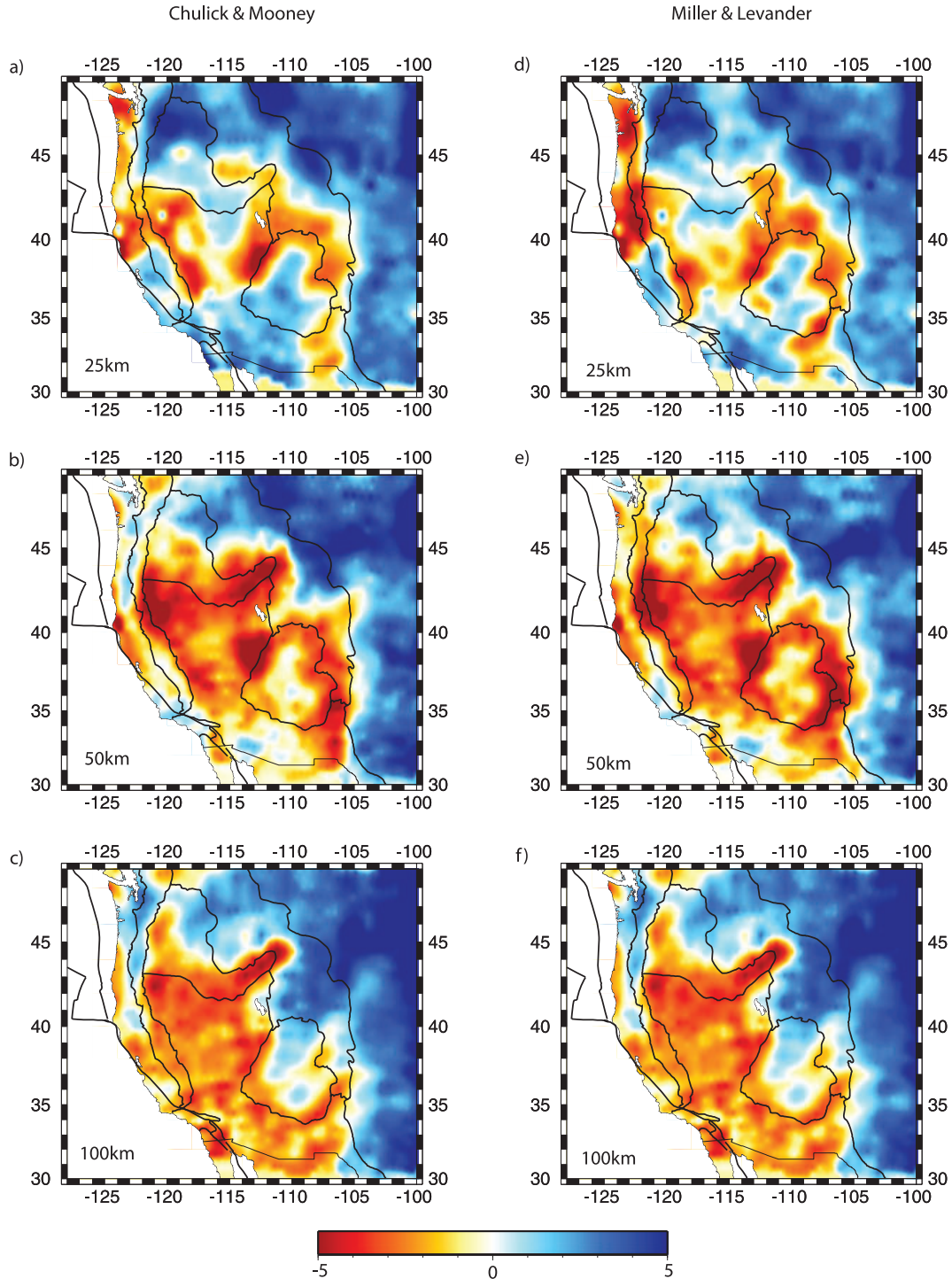
Figure 4. Comparison of the joint tomographic models obtained after applying different crustal corrections. Map views on the left-hand side (a, b and c) show the model resolved using the crust thickness estimates of Chulick & Mooney (2002). Depth is indicated in the bottom left-hand corner. The velocity model shown in map views on the right (d, e and f) was resolved using the crustal model from Miller & Levander (2009). Note that these models only slightly differ at 25 km depth (a and d) and are almost identical at greater depths.

body-waves are sensitive and account for wave front healing effects. Our tomographic method uses paraxial kernel theory to calculate the forward-scattering sensitivity kernels for teleseismic arrival times (Dahlen *et al.* 2000; Hung *et al.* 2000; Hung *et al.* 2004). Sensitivity kernels are calculated for the 0.02–0.1 Hz frequency band used in the calculation of the cross-correlograms used to determine the relative shear wave arrivals. For these teleseismic shear body-waves, the typical kernel width is ∼270 km at 600 km depth. This approach is described in more detail in Obrebski *et al.* (2010). The inversion of teleseimic shear-wave constraints using finite-frequency theory provides a tomographic model with a resolution of the order of 300 km (see resolution tests in Obrebski *et al.* 2010).

JOINT INVERSION SCHEME

The model domain is a spherical cap centred at 39.5N 112.5W. The domain extends from 127°W to 98°W and 25°N to 54°N, and from the surface to a depth of 1250 km. There are 65 nodes in the horizontal direction and 129 in the vertical direction, yielding a grid spacing of ∼40 km in the horizontal direction and ∼10 km in the vertical direction. The model box is larger than the region in which we expect to have good resolution. By using relative arrival time measurements for the body-waves we assume that the sensitivities of all arrivals for a given earthquake are the same outside the model box. Using a larger model box causes any anomalies outside the model region to be accommodated in the unresolved outer region of the model space preventing pollution of the primary target region beneath the seismic network. The finiteness of the sensitivity kernels means there is no need for smoothing. Our inversion does require damping and uses LSQR (Paige & Saunders 1982) to iterate to a final model.

The question of how to weight the body-wave and surface-wave data sets is crucial. The two data sets act as constraints on the same model, that is, the distribution of velocities anomalies δv_i, $i = 1, \ldots, M$ at each one of the M nodes of the grid. Nevertheless, these data sets have intrinsically different properties. The body-wave data set is composed of a large number of relative traveltimes δt_j, $j = 1, \ldots, N_b$ corresponding to station-event pairs. The surface-wave data set is made of a smaller set of relative phase velocities $\delta \phi_j$, $j = 1, \ldots, N_s$ estimated for 13 frequencies at each node of the grid inside the boundaries of the station array and from 0 to 300 km depth. In addition, the relative traveltimes δt_j and relative phase velocities $\delta \phi_j$ have different value ranges, that is, different variances $\sigma_{t,i}$ and $\sigma_{\phi,i}$, respectively. Therefore, without applying an adequate weighting scheme, one of the two data sets, having a larger number of elements, and/or a larger variance, would dominate the inversion scheme. To account for these differences, we use the following weighting scheme, following Julia *et al.* (2000):

$$E = \frac{p}{N_b} \sum_{i=1}^{N_b} \left(\frac{\delta t_i - \sum_{j=1}^{M} K_{b,ij} \delta v_j}{\sigma_{t,i}} \right)$$

$$+ \frac{1-p}{N_s} \sum_{i=1}^{N_S} \left(\frac{\delta \phi_i - \sum_{j=1}^{M} K_{s,ij} \delta v_j}{\sigma_{\phi,i}} \right).$$

K_b represents the sensitivity kernels of the body-waves that provide the link between the relative shear velocities δv at each node of the model and the associated relative traveltime δt. In a similar

way, K_s are the vertical sensitivity kernels for the surface-waves that link the relative phase velocity $\delta \phi$ for a certain period and at a given latitude–longitude point in our model, to the shear velocities δv at each node of the model located beneath that latitude–longitude point, from depth of 0 to 300 km. The number of relative traveltimes and phase velocities N_b and N_s, as well as their respective variance $\sigma_{t,i}$ and $\sigma_{\phi,i}$ are used to weight the different data sets in an objective fashion. The parameter p ranges from 0 to 1, and allows a manual tuning of the relative contribution of each data set. This parameter is somewhat subjective and determined mainly by visual inspection of the final model after trying different values. In this study, we chose $p = 0.7$ (Fig. 5).

The motivation of integrating body- and surface-waves in the inversion is to compensate for the lack of resolution of body-wave tomography at shallow depth, where the teleseismic body-wave rays do not cross each other. To take into account this gradual decrease in the resolution towards the surface, we multiply the body-wave kernels K_b by a ramp function that equals 1 at 60 km depth and vanishes at the surface. We chose 60 km for the lower limit of the ramp, as our tests show that the upper 50 km of the lithosphere is the region where the purely body-wave based tomographic inversion maps show short wavelength heterogeneities unique to each stations (Fig. 6). This is approximately the station separation which is ∼70 km where there are only USArray stations, and smaller where other networks are also available (Fig. 2). The surface-wave kernels K_s are not modified. This way, the upper part of the model is not affected by the intrinsically poor resolution of the body-waves at shallow depth, instead it is dominated by the surface-wave data set which provides good constraints. Station terms are included in the body-wave part of the inversion matrix to absorb traveltime delays common to each station, that is, at shallow depth directly beneath the station. Event corrections are also included to account for any baseline difference between events (VanDecar & Crosson 1990).
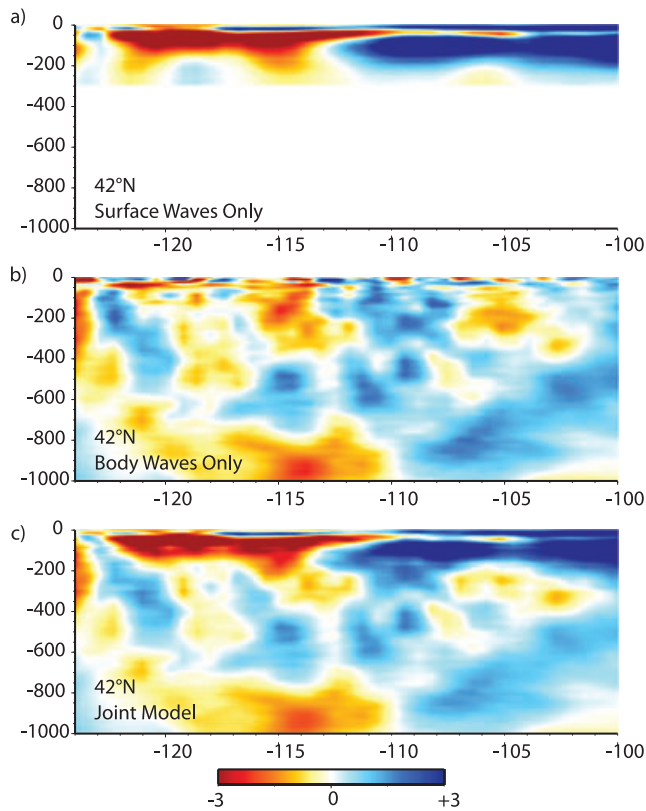
Adjustment of inversion parameters

The inversion parameters, that is, the damping factor, the allowed amplitude of the station corrections and the p parameter that balances the relative contribution of the body- and surface-wave data sets were chosen by systematically studying their effect on the model when their values are modified independently. Trade-off curves between model norm and residual misfit were used to select the appropriate damping $d = 0.04$. Several values were tried for station correction amplitudes and we chose the one that generates realistic station delay terms (Fig. 7). The parameter p has an influence on the final misfit of the body- and surface-wave data set and on the normalized rms of the model. We choose $p = 0.7$ as this value minimizes the misfit for both data sets (Fig. 5a). It also allows recovery of velocity rms values very similar to the purely surface-wave tomographic model at depth shallower than 300 km and to that of the purely body-wave tomographic model below 300 km depth (Fig. 5b). Finally, it captures the main features that appear in both the surface-wave and body-wave models (Fig. 6).

Resolution

Once combined, the body- and surface-wave data sets provide a horizontal resolution from 200 to 500 km and a vertical resolution from 10 to 500 km, depending on depth. We have performed checkerboard resolution tests using boxes with alternating high- and low-velocity of different sizes (Figs 7 and 8). These tests show that
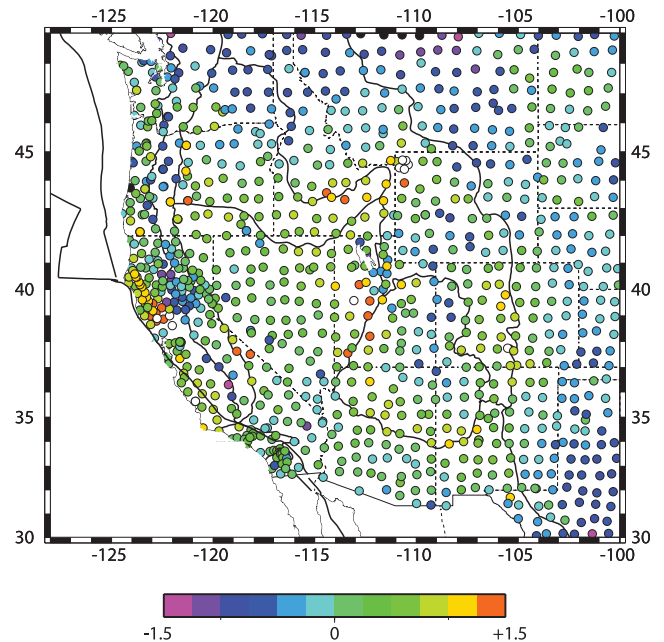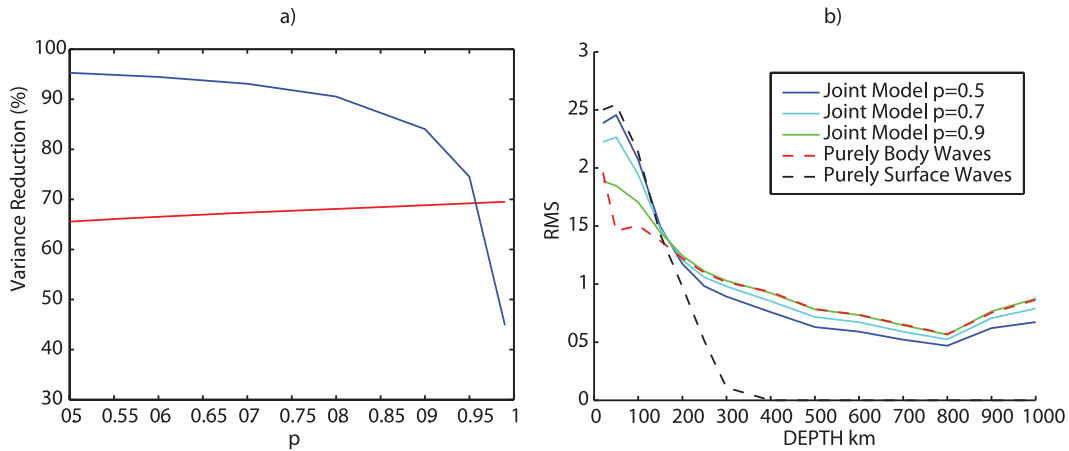
Figure 5. Dependence of the data variance reduction and velocity anomaly rms as a function of the parameter *p*. (a) Evolution of the variance reduction of the teleseismic shear-wave (red) and surface-wave (blue) data sets for values of *p* ranging from 0.5 to 1.0. (b) Normalized rms of the velocity anomalies of the joint model at depths from 50 to 1000 km for $p = 0.5$, 0.7 and 0.9. For comparison, the rms of the velocity anomalies for the models obtained by inverting just the surface-waves constraints, and just the body-wave data set are also shown (dashed lines).

Figure 6. Comparison of the surface-wave only (a), body-wave only (b) and joint model (c) using an E–W vertical cross-section at 42°N; (b) emphasizes the poor resolution provided by body-waves at depths smaller than ~150 km using the typical station spacing of USArray. In the joint model, the upper 150 km are constrained mainly by the surface-wave data set.

the resolution improves with decreasing depth due to the inclusion of shorter wavelength surface-waves. The vertical resolution is as good as 10 km in the upper 100 km, 100 to 200 km in the upper mantle and transition zone and 350 to 500 km in the lower mantle (Fig. 8). The horizontal resolution ranges from 200 to 500 km (Fig. 9).

Figure 7. Station correction terms resolved at each station for the body-wave data set.

Comparison of the joint model with the body- and surface-wave models inverted independently

Fig. 6 shows a vertical cross-section from the model obtained by inverting the body-wave data set only, the surface-wave data set only and both of them simultaneously, with a view to illustrating how the joint model is constrained by each data set. The upper 150 km of the joint model is dominated by the surface-wave constraints and the deeper part looks very similar to the body-wave model. The body-wave model has poor resolution where the ray paths do not cross each other, namely the lithosphere. In contrast, at greater depth, the body-wave model benefits from many crossing ray paths. For this reason, the already well-constrained deeper part of the model does not significantly change by including additional shallow constraints from the surface-waves. In the body-wave only model, which has little shallow resolution, the traveltime signal resulting from shallow depths is absorbed by the station terms. With the inclusion of the
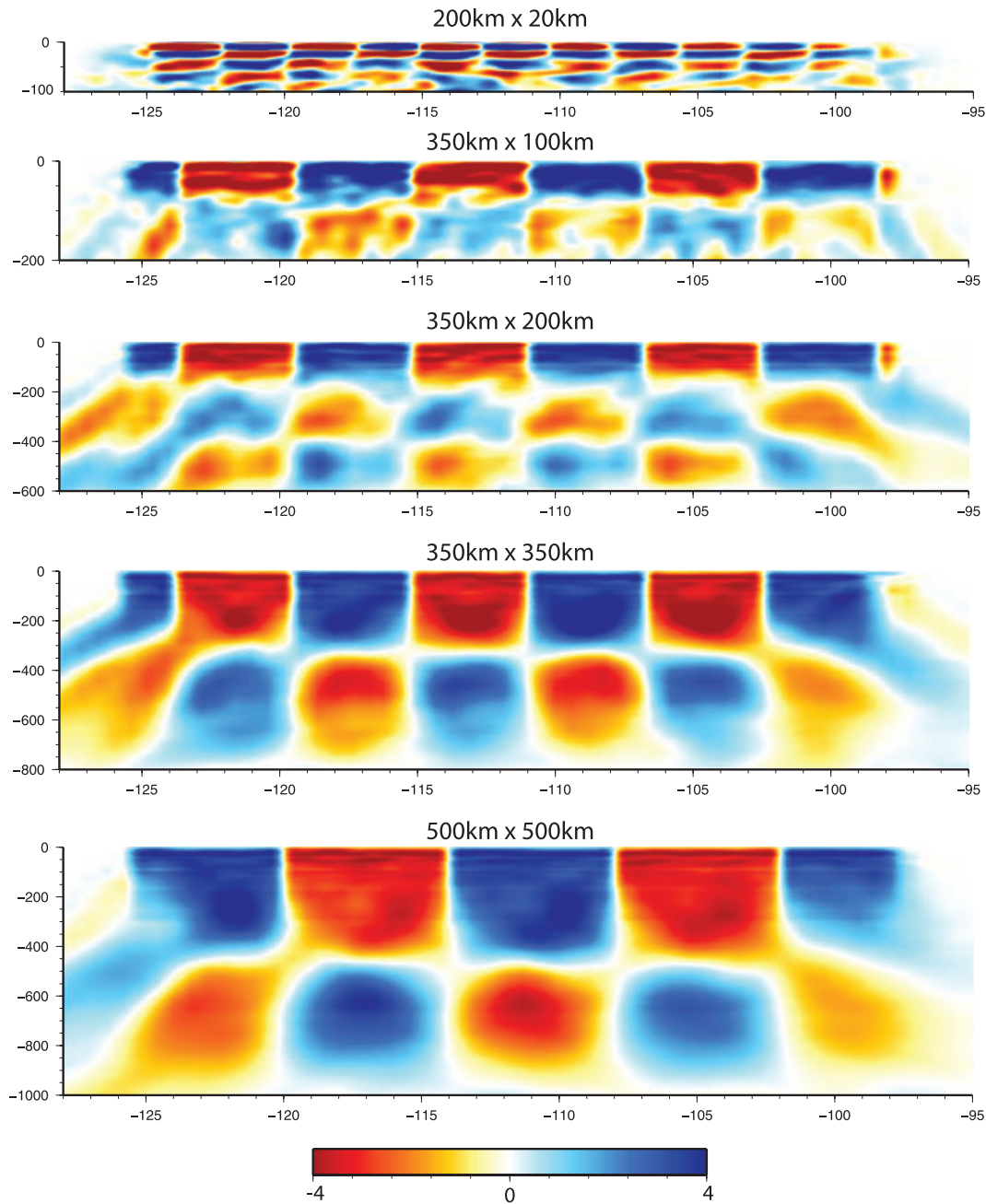
Figure 8. Checkerboard resolution tests with alternating high- and low-velocity boxes. The size of the boxes is indicated at the top of each plot. The first and second numbers are the width (in both horizontal directions) and the thickness (in depth) of the boxes. The input (synthetic) velocities anomalies were ±4 per cent. The synthetic velocity anomalies were used to calculate synthetic traveltimes and phase velocities to which random noise was added. The applied noise was derived by selecting randomly from a Gaussian distribution with a standard deviation equal to 15 per cent of the traveltime delay or phase velocity. The synthetic traveltimes and phase velocities were then combined and inverted exactly as we did for the real data. Vertical E–W slices at 41°N through the recovered velocity structures are shown. The lateral and vertical resolutions increase from the bottom to the top of the model. We use smaller boxes to illustrate the increasing resolution at shallow level. Only the well-resolved region of the model is shown and discussed in this manuscript.

surface-waves, we bring constraints on the upper 150 km, and less of the body-wave signal is absorbed into the station terms.

Body- and surface-wave tomography are both imperfect approaches with distinct resolution. Therefore, discrepancies may exist between the tomographic models retrieved from these data sets. Figs 6(a) and (b) exhibit a discrepancy between 104°W and 107°W in the upper 200 km. The surface-wave model in this area is fast while and the body-wave model is slow, although both models show slow velocities below ∼200 km depth. The reason for this discrep-

ancy is likely due to the resolution limitations when using relative body-wave traveltimes as we do. Using relative traveltimes means that we cannot capture a large horizontal anomaly that spans the array. At no time does USArray span the full west-to-east width of our model, instead it only covers a narrower swath similar in width to this discrepancy between the two models. The addition of constraints from surface-waves allows us to resolve this feature reducing the effect of this intrinsic limitation in the body-wave constraints.
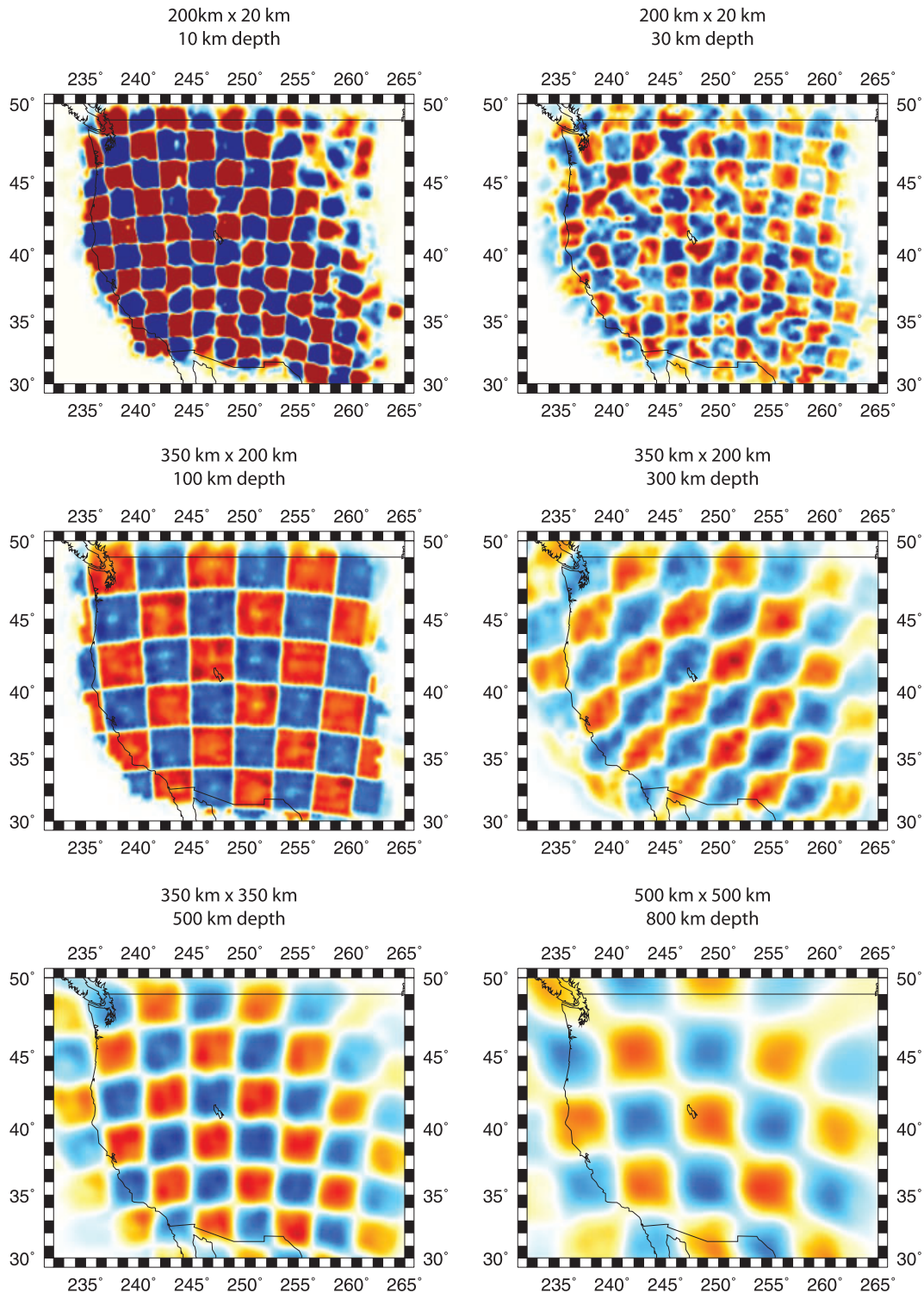
Figure 9. Same as Fig. 7, except that horizontal slices through the recovered velocity structures are shown.

RESULTS

Figs 10–13 show map views and vertical cross-sections through the main features of the western margin of the North American Plate as they are observed in our DNA10-S joint model. As expected, the deep part of our joint model is broadly consistent with other USArray-based teleseismic *P*-wave (Burdick *et al.* 2008; Roth *et al.* 2008; Burdick *et al.* 2009; Schmandt & Humphreys 2010)

and *S*-wave (Tian *et al.* 2009; Schmandt & Humphreys 2010) models. On the other hand, the uppermost part is well correlated with surface-wave tomographic models (Yang & Ritzwoller 2008; Pollitz & Snoke 2010). The improvement achieved using the joint approach concerns mainly the upper mantle. At this depth, the joint model has better lateral resolution than the surface-wave models and better vertical resolution than the body-wave models. Another important aspect is that the good resolution obtained from the surface down to
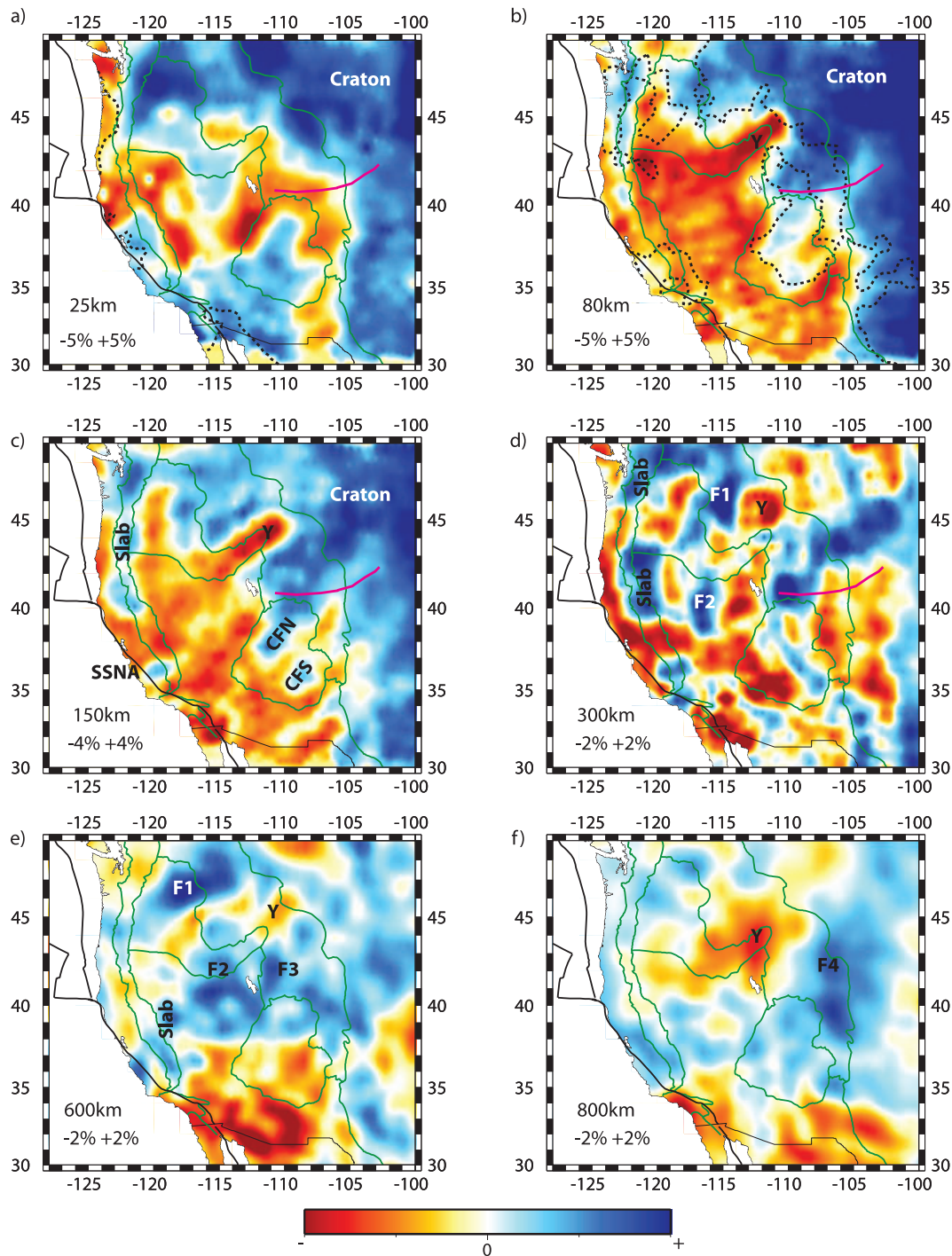
Figure 10. Constant depth map views of the model at 25, 80, 150, 300, 600 and 800 km depth. Note that the colour-scale range used to represent velocity anomalies varies from one depth plot to another and is indicated in the lower left-hand corner of each plot. The physiographic boundaries are shown in green and the Cheyenne Belt is plotted in pink. The dashed line on (a) is the 25 km depth contour for the Moho discontinuity (Chulick & Mooney 2002). Note that most of the region shown is crust with the exception of a few areas along the Pacific and Gulf of California coasts. Plot (b) shows the 80 km depth contour for the lithosphere–asthenosphere boundary (dashed line) from Miller & Levander (2009). Areas with lithosphere deeper than 80 km include a region centred on the southern Sierra Nevada, the Colorado Plateau, the Great Plains, a large portion of the Rocky Mountains, the Columbia River Plateau and the Washington coast. Plot (d) shows the numerous short-wavelength anomalies in the asthenosphere. Several fast features appear in the model east of the currently subducting slab in the Pacific Northwest and are labelled F1 to F4. Three other fast features are imaged beneath the Colorado Plateau (CFN and CFS, for Colorado Fast North and South) and beneath the Sierra Nevada (SSNA, South Sierra Nevada Anomaly). Plot (e) and (f) illustrate the smooth velocity structure of the transition zone and top of the lower mantle. A broad slow anomaly labelled Y is observed at all depths beneath the Yellowstone region.
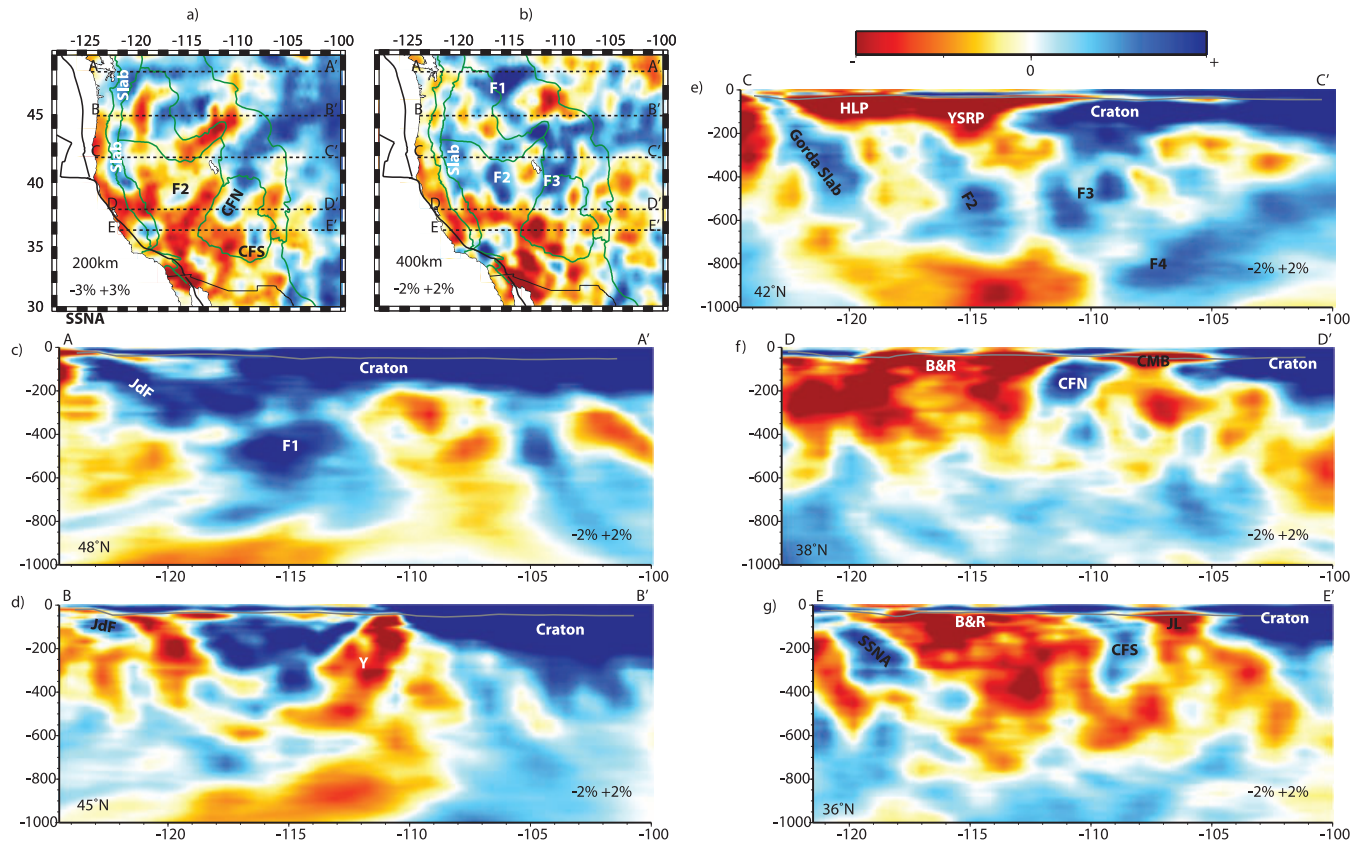
Figure 11. E–W vertical cross-sections through the DNA10-S model. Note that the colour-scale range used to represent velocity anomalies varies from one depth plot to another and is indicated on each plot. Plots (a) and (b) are map views of the model at 200 and 400 km depth that show the position of the cross-sections (c)–(g) at 48, 45, 42, 38 and 36°N. The maximum depth of the vertical cross-sections is 1000 km. The longitude is shown on the horizontal axes. The grey line is the Moho discontinuity. Cross-section (c) in northern Cascadia shows a somewhat continuous Juan de Fuca slab (JdF) that flattens at 300 km depth and connects to a broad fast anomaly observed down to 800 km. A fast shallow anomaly, indicative of intact lithosphere of the North American craton, is observed from the eastern edge of the model as far west as −116°W; (d) illustrates the weak signature of the slab below 150 km beneath Oregon. A fast block is sandwiched between slow velocities above and to the east of the weak slab on the west, and the Yellowstone anomaly (Y) on the east; (e) shows several fast anomalies (F2, F3, F4) aligned with the currently subducting Gorda slab and all located north from the southern edge of the presently subducting slab. This cross-section also shows the low velocities beneath the High-Lava Plain (HLP) and the Yellowstone-Snake River Plain (YSRP). Note that the YSRP anomaly extends deeper than the HLP, suggesting these two volcanic fields are structurally different. (f) and (g) show the structure of the Basin and Range (B&R), Colorado Plateau, Rocky Mountains and Great Plains. Low velocities are observed beneath the B&R in the asthenospheric window left by the removal of the Farallon slab. Low velocities are also found beneath the Colorado Mineral Belt (CMB) and Jemez Lineament (JL). The vertical geometry of the fast anomalies shown in Fig. 8 beneath the southern Sierra Nevada (SSNA) and also beneath the Colorado Plateau (CFN and CFS) is shown in (f) and (g) (see also Fig. 13).

the lower mantle allows a thorough visual inspection of the features which extend across the well-resolved region of both the body-wave and the surface-wave models, and that would thus be observed only partially by using these data sets independently. Compared to previous local models (Waite *et al.* 2006; Sine *et al.* 2008), the larger aperture used here allows observation of the possible link between individual lithospheric features, the adjacent tectonic provinces and the underlying deep structure of the mantle. In this section we provide a description of the main features we observe in the western United States.

Juan de Fuca-Gorda Slab and mantle fast features in the Pacific Northwest

The currently subducting Juan de Fuca-Gorda slab is imaged as a relatively weak and shallow fast seismic anomaly. In particular, the slab

has little signature beneath Oregon (Figs 10d–e and 11d) where it is not imaged beneath 150 km (Fig. 11d). In contrast, beneath Washington and California, the slab anomaly is clearly observed as deep as 400 km and 600 km, respectively. The apparent absence of slab beneath northern Oregon has been hinted before using body-wave tomography (Rasmussen & Humphreys 1988; Bostock & Vandecar 1995; Burdick *et al.* 2008; Roth *et al.* 2008; Sigloch *et al.* 2008) and does not seem to be an artefact of the method or resolution (Burdick *et al.* 2009; Obrebski *et al.* 2010). The addition of surface-wave constraints as done here further suggests that the absence of the slab is real. Beneath Washington, the slab seems to flatten (Fig. 10d and 11c) and connect to a deeper fast anomaly with similar amplitude (F1) that extends down to 800 km (Fig. 11c). The wide and continuous E–W station coverage used in this study shows how further south, around 42°N, several fast features also appear east of the currently subducting slab (F2, F3, F4, Figs 10 and 11e). The nature of these features is discussed later in this paper.
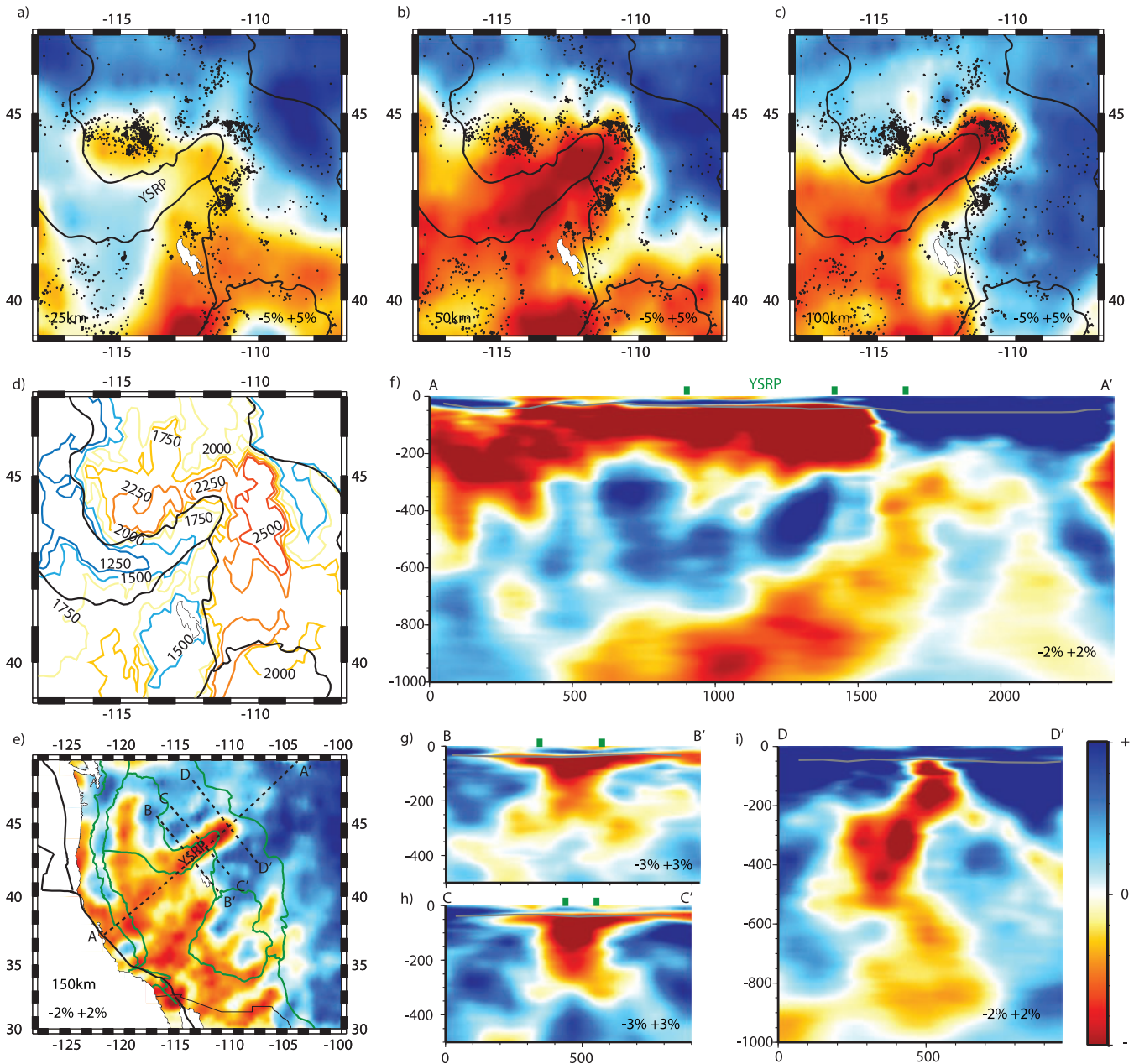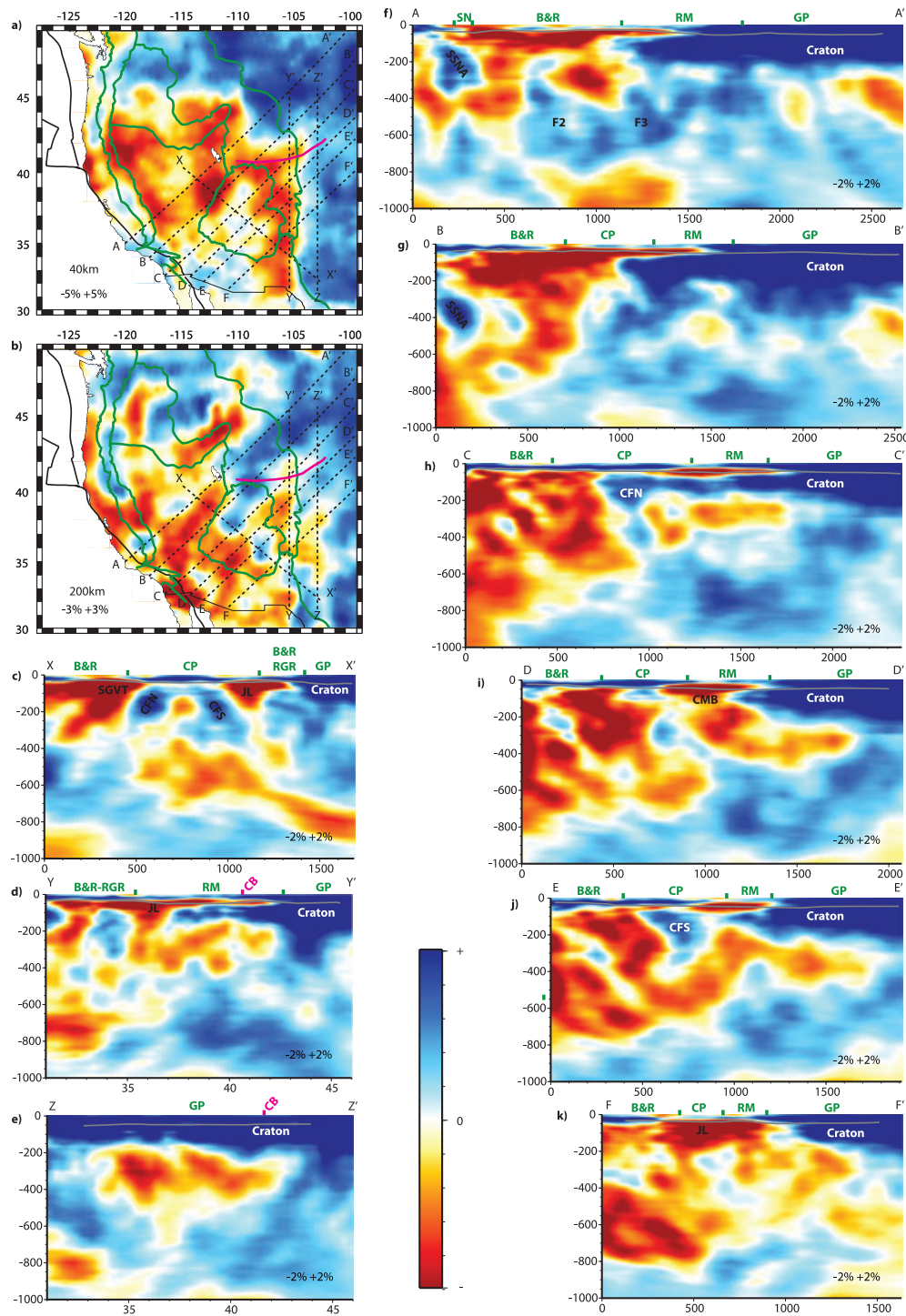
Figure 12. Map views and vertical cross-sections illustrating the shape of the Yellowstone anomaly. Note that the colour-scale range used to represent velocity anomalies varies from one depth plot to another and is indicated on each plot. Map views (a)–(c) show that the top of the Yellowstone anomaly displays a parabola shape in the upper lithosphere (25 and 50 km depth) and then an elongated finger shape directly beneath the Yellowstone-Snake River Plain at greater depths (e.g. 100 km). The lateral extent of the parabola shows correlation with the distribution of $M > 3$ local seismicity (black dots) and also with the topography as shown in (d). Plot (e) indicates the location of vertical slices along and across the Yellowstone-Snake River Plain shown in (f)–(i). Green dots on (f)–(i) mark where the slices cross the physiographic structural boundaries shown as green lines on (e). (f) and (i) show the Yellowstone anomaly as a slow feature that extends continuously from the surface down to the bottom of our model at 1000 km. The top of the anomaly in the upper 200–250 km underlies the Yellowstone-Snake River Plain and is elongated in the direction parallel to the absolute motion of the North American plate. It is stronger and deeper toward the younger calderas as in numeric models of plume-plate interaction (e.g. Lowry *et al.* 2000). The elongated shallow anomaly is connected to a more vertical low velocity anomaly located beneath the currently active Yellowstone Caldera, suggesting that this is the source for Yellowstone volcanism, and interpreted as the Yellowstone mantle plume. The plume anomaly is not a simply vertical conduit, but weaves its path to the surface around block of high velocity material interpreted as slab fragments. Plots (g) and (h) show the present-day plume head beneath the Snake River Plain. The anomaly is restricted to the upper mantle beneath the now-inactive older calderas and exhibits a mushroom shape. The anomaly flattens, becomes broader, shallower and weaker with increasing age of the hotspot-track calderas at the surface (compare g and h).

Yellowstone region

A slow anomaly is imaged beneath the YSRP region in the upper 200–250 km and is connected to a large slow body that extends

continuously from beneath the Yellowstone Caldera region down to the bottom of our model at 1000 km. Overall, the structure is consistent with that imaged previously by Obrebski *et al.* (2010) using purely *P*- and *S*-wave based tomographic inversion. The real

Figure 13. Map views and vertical cross-section showing the crust and mantle structure in the region of the Colorado Plateau (CP) and southern Rocky Mountains (RM). Note that the colour-scale range used to represent velocity anomalies varies from one depth plot to another and is indicated on each plot. Plots (a) and (b) show the location of the vertical cross-sections from A–A′ to Z–Z′. The physiographical boundaries are shown in green and the Cheyenne Belt (CB) in pink. The maximum depth of the vertical slices is 1000 km. Green and pink dots on (c)–(k) mark where the cross-sections intersect the structural boundaries shown in green and pink on (a) and (b); (c) shows the fast features CFN and CFS beneath the Colorado Plateau along with slow velocities beneath the Basin and Range (B&R) and Saint George Volcanic Trend (SGVT) to the NW and the Jemez Lineament (JL) and Rio Grande Rift (RGR) to the SE. (d) and (e) are N–S vertical slices that illustrate how the slow velocities at the eastern margin of the Colorado Plateau and southern Rocky Mountains connect with deeper slow velocities beneath the Rocky Mountains and the Great Plains (GP); (f) and (g) show the fast, likely intact North American lithosphere, that extends from the Great Plains into the Rocky Mountains. Slow upper lithospheric velocities are observed in a thin layer on the west flank of the Rocky Mountains; (f) and (g) also illustrate the geometries of the South Sierra Nevada Anomaly (SSNA) that reaches a maximum depth of 450 km; (h)–(k) further emphasize the structure of the fast (CFN and CFS) and slow anomalies (CMB, Colorado Mineral Belt and JL) in the Colorado Plateau-Rocky Mountain region. These slow anomalies connect with the large slow body shown in (d) and (e) and located to the east. The lithosphere of the southern part of the Rocky Mountains is dominantly slow, in contrast with the rest of the Rocky Mountains as shown in (f) and (g).

improvement of the current study concerns the upper part of the Yellowstone anomaly, from the surface down to 300 km, where the 3-D geometry is better defined due to the addition of short period surface-waves. Along the YSRP, the amplitude of the slow anomaly and its depth extent increase towards northeast, that is, towards the younger calderas (Fig. 12f). Bellow ∼80 km, the anomaly does not extend laterally beyond the physiographical boundaries of the YSRP (Figs 10b and c and 12g–i). Above this depth, in the uppermost mantle, the Yellowstone anomaly spreads laterally (Figs 12g and h) beneath the Moho discontinuity. Seen in map view (Figs 10a and 12a and b), the boundary of the slow anomaly has a parabola shape that is centred on the YSRP axis and that grows wider towards the SW, that is, in the direction of increasing age of the calderas. In the crust, the velocity distribution exhibits a similar parabola-shaped pattern. However, at the older southwestern end of the YSRP the crust displays fast seismic velocities (Fig. 12a).

Basin and Range

The crust of the Basin and Range is divided into two domains, with slow velocity to the north and high velocity to the south, the boundary being roughly the southern tip of the Sierra Nevada (36°N). The slowest anomalies are located at the western and eastern edge of the Great Basin (Fig. 10a). Below 40 km, the Basin and Range is uniformly slow and these slow velocities are continuous with other slow regions beneath the active western United States (Figs 10b and c).

Colorado Plateau

The lower crust of the Colorado Plateau exhibits a relatively simple structure (Fig. 10a). It is dominantly fast with the exception of the Cenozoic volcanic areas: Colorado Mineral Belt (CMB), Saint George Volcanic Trend (SGVT) and Jemez Lineament (JL) (Fig. 1). The mantle is heterogeneous in terms of seismic velocities, with a large portion being slow (Figs 10, 12 and 13). This observation is consistent with the pre-USArray regional studies of Lee & Grand (1996) and 2-D profiles of Sine *et al.* (2008). Only the northern part (CFN) and a rounded spot in the southeastern part (CFS) of the Colorado Plateau exhibit a distinctive fast anomaly (Figs 10b and c). CFN reaches 300 km (or perhaps 500 km, Fig. 11f) and CFS reaches 400 km (Fig. 11g). These vertically elongated features are likely not due to either anisotropy, as similar features appear in our previous *P*-wave model (Obrebski *et al.* 2010), or smearing along the ray paths, as the Colorado Plateau is located in a well-resolved area of our model. The distribution of low velocities seems to reflect a shallow lithosphere–asthenosphere boundary (LAB). Receiver functions estimates of the LAB depth range from 50 to 80 km on the margin of the Colorado Plateau where we find low mantle velocities, and from 80 to 130 km where we image the fast features CFN and CFS (Fig. 10b).

Rio Grande Rift and volcanic fields around the Colorado Plateau

From the eastern edge of the Colorado Plateau to the western edge of the Great Plains, in the crust and upper mantle, a broad slow anomaly spans the major Cenozoic volcano-tectonic features. At 25 km and 80 km (Figs 10a and b), the model shows a N–S elongated strip of low velocities beneath the Rio Grande Rift. This anomaly overlaps with two NE–SW elongated slow 'fingers' that align with the location of the CMB and the JL (Fig. 1). To the north, very low velocities (negative anomalies lower than –2 per cent) are found as deep as 100 km beneath the CMB (Figs 11f and 13i). To the south, very low velocities are found as deep as 150 km beneath the JL (Figs 11g and 13c, d and k). Similar low velocities were observed in the regional *P*-wave model of Humphreys *et al.* (2003). The large array aperture used in this study allows imaging of how the slow velocities beneath the Cenozoic volcanic fields are connected to broad slow anomalies around and beneath them. The very low lithospheric anomalies beneath the CMB and JL are underlain by low-velocity (negative anomaly larger than –2 per cent) material in the asthenosphere and in part of the transition zone. The slow anomalies beneath these two volcanic fields seem to be connected to the low velocities observed beneath the Basin and Range to the west. The low velocities beneath the CMB and JL also connect with a large low-velocity anomaly spanning the upper mantle and the transition zone, and located beneath the southern Rocky Mountains and the Great Plains (Figs 10d and e, 11f and g and 13d, e and 13i–k).

Rocky Mountains

The lithosphere–asthenosphere velocity structure of the Rocky Mountains shows three domains: the southern Rockies (south of ∼42°N) and the central/northern Rockies that can be split into an eastern and a western domain. The crust and upper mantle of the southern Rockies is dominantly slow (Figs 10a–d). The crust and upper mantle of the eastern side of the central and northern Rockies are uniformly fast with high anomalies (>2 per cent) down to 200–300 km (Figs 10a–d and 13f and g). The structure of the western side of the central and northern Rocky Mountains is more complex. The crust and upper mantle there is dominantly very fast (>2 per cent) down to 200–300 km (as on the eastern side) with the exception of a strip of low velocities in the lower crust. This slow region extends from the Idaho-Washington-Oregon border southwards and connects with the low velocities of the southern Rocky Mountains domain (Figs 10a and 13). The N–S velocity contrast in the mantle is well observed at 80, 150 and even 300 km depth (Figs 10b–d).

Transition zone and lower mantle

The structure of the transition zone is marked by a strong north–south contrast with fast velocities blocks (F1, F2 and F3) that dominate the northern part of the model (Fig. 10e) and slow material to the south. The east–west fast-to-slow boundary occurs a little south of the current location of the Mendocino Triple Junction that separates ongoing subduction beneath the Cascades from transform motion along the San Andreas Fault (Fig. 1). Several localized slow spots are observed in the northern half of the model, including the region just north of the Yellowstone Caldera. To the south of the model, where the transition zone is dominantly slow, there is an elongated fast feature with a roughly NW–SE orientation just east of the Rocky Mountain Front. This feature was previously observed by Sigloch *et al.* (2008). Deeper in the model, for example, 800 km (Fig. 10f), the top of the lower mantle exhibits a smooth long wavelength velocity structure that is dominantly fast with the exception of a broad slow region centred beneath Yellowstone.

DISCUSSION

Lateral and vertical extent of the cratonic region

The good resolution achieved from the surface down to the transition zone allows better constraints on the lateral and vertical extent of the North American Craton. In the upper mantle (Figs 10a–d), a sharp SW–NE contrast exists between the cratonic area that exhibits fast velocities deeply rooted in the upper mantle and the active western United States that is underlain by slow velocities potentially indicative of hot, shallow asthenosphere. The small-scale geometry of the cratonic margin is less obvious, as pointed out by previous tomographic studies (Lee & Grand 1996; van der Lee & Nolet 1997; Henstock *et al.* 1998; Humphreys *et al.* 2003). As expected, a broad region of fast uppermost mantle is observed beneath the stable Great Plains (Figs 10b and c). Fast anomalies >2 per cent extend to 200–300 km depth (Figs 10, 11 and 13), which are consistent with global estimates for the thickness of the cratonic continental lithosphere (Gung *et al.* 2003) and with the ∼250 km estimate for the central US craton (Grand 1994). Nevertheless, this 200–300 km thick fast region also extends westwards beyond the Rocky Mountain Front, that is, into the western active part of the United States (Figs 10 and 13). It is also connected to a deeply rooted fast mantle beneath the northern part of the Colorado Plateau (anomaly CFN). Fig. 10(b) illustrates the geographical correlation between the broad area where the upper 200 km of the mantle exhibits higher seismic velocities and the regions where the analysis of converted *S*-to-*P* phases observed in receiver functions suggest that the LAB is deep (Fig. 10b). All these observations suggest that thick, mainly intact continental lithosphere exists not only beneath the stable Great Plains, but also farther west into the active Rocky Mountains and perhaps part of the Colorado Plateau.

Mantle plume beneath the Yellowstone region

We interpret the large anomaly imaged from the surface down to the bottom of our model (1000 km) beneath the Yellowstone hotspot track as a hot and buoyant whole mantle plume that feeds the volcanism in the YSRP region. The broad mantle geometry of the Yellowstone anomaly as imaged in Fig. 12(f) is similar to that predicted by numerical models of the interaction between an impinging plume and an overriding moving plate (Lowry *et al.* 2000; Steinberger *et al.* 2004). In addition, the parabolic shape of the head (Fig. 12b) is consistent with numerical model of a flattening plume beneath a moving plate (Ribe & Christensen 1994). The presence of a whole mantle plume beneath the YSRP is also suggested by geometric (time progressive sequence of silicic volcanism parallel to the absolute motion of the north American plate) and chemical (high ^{3}He/^{4}He ratio) anomalies.

The detailed velocity structure of the shallowest part of the Yellowstone anomaly as observed in our joint model also highlights the correlation with the geophysical, seismotectonic and physiographic properties of the Yellowstone-Snake River Plain. The parabola-shaped anomaly observed in the crust and mantle lithosphere down to ∼80 km coincides with the region of higher topography and lower Bouguer anomaly (Fig. 12d). This suggests that this slow material is also less dense and provides the positive buoyancy necessary to sustain isostatically the high topography in the YSRP region. Slow velocities in the crust may result from heating due to the invasion of hot material from the plume beneath the Moho that did not lead to volcanism, dehydration and densification, and that is thus still

providing extra buoyancy and higher isostatically sustained topography. In contrast, within the YSRP, heating of the crust by the same Yellowstone plume did produce volcanism. Rock dehydration, and subsequent post-volcanism cooling may explain the fast crustal velocities in the older, southwestern part of the YSRP, where the heat flow is also lower than in northeastern end of the YSRP. These potentially denser rocks provide negative buoyancy that tend to compensate partially the positive buoyancy of the underlying broad Yellowstone plume and then account for the locally lower topography and higher Bouguer anomaly. Finally, the outer boundary of the parabola-shaped low-velocity body in the upper 25–80 km of the crust–upper mantle correlates with the location and distribution of local seismicity. A possible interpretation is that the invasion of the Yellowstone plume generates sufficient strain and deviatoric stresses in the lithosphere on the outer rim of the topographic uplift to trigger seismicity.

Slab graveyard beneath the Pacific Northwest

The shortness of the currently subducting Juan de Fuca-Gorda Plate and the presence of several fast features east of it suggest that the slab has undergone substantial fragmentation. The F1 anomaly may be the continuation of the present-day slab (Fig. 11c). Alternatively, F1 could be a remnant of the Farallon slab separated from the currently subducting Juan de Fuca slab as a consequence of the accretion of the Siletzia terrane around 55 Ma and the associated westward trench jump (Schmandt & Humphreys 2011). At 45°N (Fig. 11d), another large fast anomaly is imaged to a depth of ∼300 km at latitudes from 118°W to 113°W, that is, east of the currently subducting slab and west of the Yellowstone plume. The eastern part of this anomaly is located east of the 0.706 line (Fig. 1), on autochthonous basement, and is separated from the fast velocities beneath the cratonic Great Plains by the Yellowstone plume. This block may therefore be the North American lithosphere separated from the rest of the craton by the intrusion of Yellowstone plume material into the lithosphere. To the south, three other large features are observed in and close to the transition zone (F2, F3 and F4, Figs 10 and 11e). West *et al.* (2009) proposed that F2 is dripping lithosphere. All these fast features are located north of an eastward extension of the current location of the Mendocino Fracture Zone that separates ongoing subduction beneath the Cascades from transform motion along the San Andreas Fault. Consequently, we rather interpret F2, and also F3 and F4 as fragments of the Farallon slab that are sitting in the transition zone adjacent to the Pacific Northwest (Figs 10e and f). Sigloch *et al.* (2008) image two fast features ('S1' and 'S2', their Fig. 1 cross-section at 42°N) that closely coincide with the location of F2–F3 and F4, and that they also interpret as fragments of the subducted Farallon slab.

Lithospheric removal beneath the Colorado Plateau

The lithospheric structure of the Colorado Plateau block is found to be heterogeneous in terms of seismic velocities, and a large portion of it is slow, suggesting a substantial amount of the former lithospheric root has been removed. The Proterozoic Colorado Plateau contrasts with the Basin and Range to the west, the Rio Grande Rift to the east and the Rocky Mountains to the north, as it has neither been significantly deformed during Laramide contraction and post-Laramide extension nor affected by the voluminous and widespread mid-Tertiary magmatism (23–40 Myr ago) of the 'ignimbrite flare-up'. We would thus expect the lithospheric root of the

Colorado Plateau to be homogeneously stronger than the tectonic provinces that surround it. The lower crust is apparently strong and intact as indicated by fast velocities (Fig. 10a), the local seismicity that extends deep into the lower crust (Wong & Humphrey 1989) and the low heat flow. Nevertheless, with the exception of the fast features CFN and CFS (Fig. 10c), there is little evidence for a strong, deep and intact lithospheric root. This observation contrasts with the evidence from Colorado Plateau xenoliths, which suggests that at 30–20 Ma the Colorado Plateau had a cool root extending to depths of up to 140 km (Riter & Smith 1996). Therefore, even if part of the Colorado Plateau root still persists, it seems that a large part of it has been removed.

The isolated fast features CFN and CFS could represent the remnant cold core of the lithospheric root of the Colorado Plateau resulting from the combined effects of conductive heat transfer towards the centre of the Colorado Plateau (Roy *et al.* 2009) and edge-driven convection (van Wijk *et al.* 2010). Nevertheless, CFN and CFS extend beyond the typical depth of continental lithosphere. Alternatively, CFN and CFS may be examples of lithospheric instabilities. Based on numeric simulation, van Wijk *et al.* (2010) showed that edge-driven convection can trigger downwelling of the cold lithospheric root of the Colorado Plateau at locations close to where we image the fast features CFN and CFS. Peaks in the residual uplift calculated by Roy *et al.* (2009) correlate with the locations of CFN and CFS. This is consistent with an advance phase of dripping and the associated rebound as described by Göğüs & Pysklywec (2008). In the lithospheric dripping process, the elevation is initially reduced, but once some of the lithospheric material detaches from the drip, isostatic uplift is expected. We therefore interpret the columnar CFN and CFS high velocities as lithospheric drips from which some lithosphere has already detached generating the uplift pattern as mapped by Roy *et al.* (2009). In the case of CFN, the spherical high-velocity anomaly directly below CFN at 300–500 km depth (Fig. 11f) may be the detached lithosphere.

Several other possible examples of post-Laramide lithospheric drips have been documented in the western United States such as the South Sierra Nevada anomaly (SSNA in Figs 10c and d, 11g, 13f and g; see Zandt *et al.* 2004) and the Central Nevada anomaly (F2 in Fig. 11, see West *et al.* 2009). Lithospheric dripping may thus be a common type of instability where the North American lithosphere was modified by its Laramide contact with the cold and hydrated Farallon slab.

High topography of the western United States

A large portion of the western United States exhibits high topography, low Bouguer anomaly and is apparently underlain by low-velocity crust and/or mantle. These observations suggest the mantle is locally hot and buoyant enough to isostatically sustain part of the high elevations. Beneath the extending Basin and Range, the high topography is probably linked to the low velocities that are widespread below 40 km. The higher topography along the western side of the central and northern Rocky Mountains could be partially supported by the strip of low velocities we image in the lower crust. The effect of dehydration of the slab on the overlying North American Plate, in particular the generation of positive buoyancy (compositional and thermal) in the lithosphere, has been proposed before (Humphreys *et al.* 2003; Humphreys 2009), but prior to this study had not been imaged. South of the Cheyenne Belt, current higher topography compared to the rest of the Rocky Mountains

is consistent with both the crust and the upper mantle being slow, providing more positive buoyancy than in the central and northern Rockies, and sustaining the higher topography and lower Bouguer anomaly. Further east, a large low-velocity anomaly is observed in the upper mantle and in the transition zone beneath the westernmost part of the Great Plains (Figs 10d and e, 11f and g, 13d and e and i-k). This region has experienced uplift and tilting since the middle Miocene (Heller *et al.* 2003) that might be related to the presence of the low seismic velocities at mantle depth.

Role of inherited structures in recent tectonic history

Our regional model shows that in several areas of the western United States, very low-velocity anomalies coincide with ancient structural boundaries that have been repeatedly reactivated. Around the Colorado Plateau, the slow lithospheric velocities that coincide with the Cenozoic volcanic fields (CMB and JL, Figs 1 and 13) have been observed before using *P*-wave tomography and were interpreted as evidence of partial melting and high temperature (Humphreys *et al.* 2003). Our model shows how these low velocities also connect with a wide slow anomaly that spans the asthenosphere and the transition zone (Fig. 13). This slow and potentially hot material may thus have been providing heat at a regional scale. Nevertheless, it is only along the Precambrian sutures that the heated lithosphere actually produced melt. This observation is in agreement with the conclusions of Karlstrom & Humphreys (1998) who proposed that the volcano-tectonic activity around the Colorado Plateau preferentially occurs along the weak and more fertile ancient structures. In the Basin and Range, the slowest anomalies in the crust (Fig. 10a) are located on the eastern edge of the Great Basin, at the structural boundary with the Colorado Plateau and Rocky Mountains. The very low velocities (<−2 per cent) observed coincide with the Saint George Volcanic Trend and could be related to the reactivation of the northern boundary of the transition between the 1.8–1.6 Ga Mojave and Yavapai Provinces (Karlstrom & Humphreys 1998). Very low velocities are also observed along the western margin on the Basin and Range, on the eastern side of the Sierra Nevada and Klamath Mountains. These may be associated with the suture between the Mesozoic accreted and plutonic terranes and the Basin and Range. Alternatively, these low velocities may also reflect deeply rooted shearing along the East California Shear Zone–Walker Lane Belt (Fig. 1) that accommodates roughly one-quarter of the Pacific–North America relative motion (Dixon *et al.* 1999).

Differences in the age and composition of the Precambrian terrains that compose the North American Plate also seem linked to the current distribution of velocities and the locus of recent tectonism. In contrast with the northern and central US Rocky Mountains that appear as a westward extension of the fast, deeply rooted cratonic lithosphere, the southern Rockies and the Colorado Plateau exhibit a distinctive slow signature. This N–S velocity contrast (at ~42°N) closely matches the compositional discontinuity across the Cheyenne Belt, which separates repeatedly deformed and magmatically intruded Precambrian basement to the south from comparatively stable Archean basement to the north.

Dynamics of the Rocky Mountains

The lithospheric structure of the northern and central Rocky Mountains is consistent with the Laramide upper-crust orogenic shortening being accommodated by a lower crust detachment, leaving the rest of the lithosphere intact. The mantle lithosphere in this portion

of the Rocky Mountains is probably strong as suggested by flexural modelling (Lowry & Smith 1994), low heat flow and also fast velocities as imaged in our model. It may not have been deformed greatly during Laramide orogeny. Humphreys (2009) suggested that the upper crust shortening may have been accommodated by a lower crust detachment, although he did not image such a structure. Our model does show a strip of low-velocity material sandwiched between the fast upper crust and the mantle lithosphere of the Rocky Mountains on their western side beneath Idaho, Wyoming and northeast Utah (Figs 10b and c and 13f–h). These low velocities could represent a weak lower crust zone hosting a detachment. In contrast, south the Cheyenne Belt, where the Rocky Mountains overlap with the Rio Grande Rift, the CMB and the JL, the whole lithosphere is slow (Figs 13i–k), suggesting it has been uniformly modified and deformed.

CONCLUSIONS

Our multiphase model with enhanced resolution at lithospheric depth allows us to image in great detail crustal, lithospheric and sublithospheric mantle structures and processes beneath the western United States. This provides improved resolution of the detailed contrast between the active western United States and the stable eastern cratonic area. In the east, fast and generally intact lithosphere extends as deep as 200–250 km, while slow velocity anomalies are widespread beneath the western United States at normal lithospheric depths and correlate with low Bouguer anomalies and high topography. These slow anomalies probably reflect hot and low-density material that provides positive buoyancy to isostatically support the high topography of a large portion of the western United States.

A continuous low-velocity anomaly, rooted below the transition zone, weaves its way between high-velocity bodies and intrudes the North American lithosphere in the Yellowstone region. The geometry of this slow body is consistent with a whole mantle plume feeding the Cenozoic volcanism in the region. The present-day head of the plume-like feature beneath the Snake River Plain is imaged to shallow and spread laterally to the southwest. Its location and geometry is consistent with the parabola-shaped high topography and seismicity implying it is responsible for uplifting the region through its low density.

The bottom of the currently subducting Gorda-Juan de Fuca slab is surprisingly shallow and uneven. North of the Mendocino Triple Junction, the mantle contains several high-velocity blocks aligned with the currently subducting Juan de Fuca-Gorda slab. We interpret these fast features as a sequence of remnant slab fragments from the former massive Farallon slab that currently sits in the transition zone.

Portions of the lithospheric root of the Colorado Plateau are found to be missing. Having been surrounded by shallow and hot asthenosphere since Oligocene time, the lithospheric root is apparently foundering in the form of drips that we image as two vertically elongated fast bodies. The dripping hypothesis is also consistent with the two peaks in surface elevation that are found immediately above the drips.

The composite structure of the western United States that has repeatedly exerted control on the distribution of tectonism and magmatism is reflected by the velocity structure of the crust and upper mantle. In our model, the slowest anomalies and the strongest velocity contrasts correlate with old tectonic and compositional bound-aries. This implies a strong influence of fossil tectonic features on new deformation processes.

REFERENCES

Bostock, M.G. & Vandecar, J.C., 1995. Upper mantle structure of the northern Cascadia subduction zone, *Can. J. Earth Sci.,* **32,** 1–12.

Burdick, S. *et al.* 2008. Upper mantle heterogeneity beneath north America from travel time tomography with global and USArray transportable array data, *Seism. Res. Lett.,* **79**(3), 384–392.

Burdick, S. *et al.* 2009. Model update December 2008: upper mantle heterogeneity beneath north America from travel time tomography with global and USArray transportable array data, *Seism. Res. Lett.,* **80**(4), 638–645.

Camp, V. E. & Ross, M. E., 2004. Mantle dynamics and genesis of mafic magmatism in the intermontane Pacific Northwest, *J. geophys. Res.,* **109,** B08204, doi:10.1029/2003JB002838.

Christiansen, R.L., Foulger, G.R. & Evans, J.R., 2002. Upper-mantle origin of the Yellowstone hotspot, *Geol. Soc. Am. Bull.,* **114,** 1245–1256.

Chulick, G.S. & Mooney, W.D., 2002. Seismic structure of the crust and uppermost mantle of North America and adjacent oceanic basins: a synthesis, *Bull. seism. Soc. Am.,* **92,** 2478–2492, doi:10.1785/0120010188

Dahlen, F.A., Hung, S.H. & Nolet, G., 2000. Fréchet kernels for finite-frequency traveltimes–I. Theory, *Geophys. J. Int.,* **141,** 157–174.

DeCelles, P.G., 2004. Late Jurassic to Eocene evolution of the Cordilleran thrust belt and foreland basin system, western U.S.A., *Am. J. Sci.,* **304,** 105–168, doi:10.2475/ajs.304.2.105.

Dickinson, W.R., 1997. Tectonic implications of Cenozoic volcanism in coastal California, *Geol. Soc. Am. Bull.,* **109,** 936–954.

Dixon, T.H., Miller, M., Farina, F., Wang, H. & Johnson, D., 1999. Presentday motion of the Sierra Nevada block and some tectonic implications for the Basin and Range province, North American Cordillera, *Tectonics,* **19,** 1–24; doi:10.1029/1998TC001088.

Dumitru, T.A., Gans, P.B., Foster, D.A. & Miller, E.L., 1991. Refrigeration of the western Cordilleran lithosphere during Laramide shallow-angle subduction, *Geology,* **19,** 1145–1148, doi:10.1130/0091–7613(1991)019<1145:ROTWCL>2.3.CO;2.

English, J.M., Johnston, S.T. & Wang, K., 2003. Thermal modelling of the Laramide Orogeny: testing the flat-slab subduction hypothesis, *Earth planet. Sci. Lett.,* **214,** 619–632, doi:10.1016/S0012–821X(03)00399–6.

Forsyth, D. W. & Li., A., 2005. Array-analysis of two-dimensional variations in surface wave phase velocity and azimuthal anisotropy in the presence of multipathing interference, in *AGU Geophysical Monograph 187,* pp. 81–98, eds Levander, A. & Nolet, G., Washington, DC

Forsyth, D.W., Webb, S.C., Dorma, L.M. & Shen, Y., 1998. Phase velocities of Rayleigh waves in the MELT Experiment on the East Pacific Rise, *Science,* **22,** 1235–1238.

Friederich, W. & Wielandt, E., 1995. Interpretation of seismic surface waves in regional networks: joint estimation of wavefield geometry and local phase velocity. Method and numerical tests, *Geophys. J. Int.,* **120,** 731–744.

Friederich, W., Hunzinger, S. & Wielandt, E., 2000. A note on the interpretation of seismic surface waves over three-dimensional structures, *Geophys. J. Int.,* **143,** 335–339.

Göğüs, O. & Pysklywec, R.N., 2008. Near surface diagnostics of dripping or delaminating lithosphere, *J. geophys. Res.,* **113,** B11404, doi:10.1029/2007JB005123.

Grand, S.P., 1994. Mantle shear structure beneath the Americas and surrounding oceans. *J. geophys. Res.,* **99,** 11 591–11 621, doi:10.1029/94JB00042.

Gung, Y.C., Panning, M. & Romanowicz, B., 2003. Anisotropy and lithospheric thickness, *Nature,* **422,** 707–711.

Heller, P. L., Dueker, K. & McMillan, M., 2003. Post-paleozoic alluvial gravel transport as evidence of continental tilting in the U.S. Cordillera, *Geol. Soc. Am. Bull.,* **115**(9), 1122–1132, doi:10.1130/B25219.1

Henstock, T. & the Deep Probe Working Group, 1998. Probing the Archean and Proterozoic lithosphere of western North America, *GSA Today,* **8,** 1–17.

Humphreys, E., 2009. Relation of flat subduction to magmatism and deformation in the western United States, in *Backbone of the Americas: Shallow Subduction, Plateau Uplift, and Ridge and Terrane Collision,* eds Kay, S.M., Ramos, V.A. and Dickinson, W.R., Geological Society of America Memoir 204, doi: 10.1130/2009.1204(04).

Humphreys, E.D., Dueker, K.G., Schutt, D.L. & Smith, R.B., 2000. Beneath Yellowstone: evaluating plume and nonplume models using teleseismic images of the upper mantle, *GSA Today,* **10**(12), 1–7.

Humphreys, E., Hessler, E., Dueker, K., Erslev, E., Farmer, G.L. & Atwater, T., 2003. How Laramide-age hydration of North America by the Farallon slab controlled subsequent activity in the western U.S., *Inter. Geol. Rev.,* **45,** 575–595, doi:10.2747/0020–6814.45.7.575.

Hung, S.H., Dahlen, F.A. & Nolet, G., 2000. Fréchet kernels for finite-frequency traveltimes–II. Examples, *Geophys. J. Int.,* **141,** 175–203.

Hung, S.H., Shen, Y. & Chiao, L.Y., 2004. Imaging seismic velocity structure beneath the Iceland hot spot: a finite frequency approach, *J. geophys. Res.,* **109,** B08305, doi:10.1029/2003JB002889.

Julia, J., Ammon, C.J., Herrmann, R.B. & Correig, A.M, 2000. Joint inversion of receiver function and surface wave dispersion observations, *Geophys. J. Int.,* **143,** 99–112.

Karlstrom, K.E. & Humphreys, E.D., 1998. Persistent influence of Proterozoic accretionary boundaries in the tectonic evolution of southwestern North America: interaction of cratonic grain and mantle modification events, Rocky Mountain, *Geology,* **33,** 161–179.

Lee, D. & Grand, S.P., 1996. Upper mantle shear structure beneath the Colorado Rocky Mountains, *J. geophys. Res.,* **101,** 22 233–22 244.

Livaccari, R.F. & Perry, F.V., 1993. Isotopic evidence for preservation of lithospheric mantle during the Sevier–Laramide orogeny, western U.S., *Geology,* **21,** 719–722.

Lowry, A.R. & Smith, R.B., 1994. Flexural rigidity of the Basin and Range–Colorado Plateau–Rocky Mountain transition from coherence analysis of gravity and topography, *J. geophys. Res.,* **99,** 20 123–20 140.

Lowry, A.R., Ribe, N.M. & Smith, R.B., 2000. Dynamic elevation of the Cordillera, western United States, *J. geophys. Res.,* **105**(B10), 23 371–23 390.

McCrory, P.A., Blair, J.L., Oppenheimer, D.H. & Walter, S.R., 2006. Depth to the Juan de Fuca slab beneath the Cascadia subduction margin–A 3-D model sorting earthquakes, U.S. Geological Survey, *Data Series 91.*

Masters, G., Johnson, S., Laske, G., Bolton, H. & Davies, J.H., 1996. A shear-velocity model of the mantle, *Phil. Trans.: Math. Phys. Eng. Sci.,* **354,** 1385–1411.

Mégnin, C. & Romanowicz, B., 2000. The 3D shear velocity structure of the mantle from the inversion of body, surface and higher mode waveforms, *Geophys. J. Int.,* **143,** 709–728.

Miller, M.S & Levander, A., 2009. Receiver Function Images of the Western US Lithosphere, *Earthscope OnSite Newsletter,* **4,** 2–3.

Morgan, W.J., 1971. Convection plumes in the lower mantle, *Nature,* **230,** 42–43.

Obrebski, M., Allen, R.M., Xue, M. & Hung, S.-H., 2010. Slab-plume interaction beneath the Pacific Northwest, *Geophys. Res. Lett.,* **37,** L14305, doi:10.1029/2010GL043489.

O'Driscoll, L.J., Humphreys, E.D. & Saucier, F., 2009. Subduction adjacent to deep continental roots: enhanced negative pressure in the mantle wedge, mountain building and continental motion, *Earth planet. Sci. Lett.,* **280,** 61–70, doi:10.1016/j.epsl.2009.01.020.

Paige, C.C. & Saunders, M.A. 1982. LSQR: An algorithm for sparse linear equations and sparse least squares, *TOMS,* **8,** 43–71

Pierce, K.L. & Morgan, L.A., 1992. The track of the Yellowstone hotspot: volcanism, faulting, and uplift, in *Regional Geology of Eastern Idaho and Western Wyoming,* pp. 1–53, eds Link, P. K., Kuntz, M. A. and Platt, L.B., Geological Society of America Memoir 179.

Pierce, K.L., Morgan, L.A. & Saltus, R.W., 2000. Yellowstone plume head: postulated tectonic relations to the Vancouver slab, continental boundaries and climate, Open-File Report 00-498, U.S. Geological Survey.

Pollitz, F.F., 1999. Regional velocity structure in northern California from inversion of scattered seismic surface waves, *J. geophys. Res.,* **104,** 15 043–15 072.

Pollitz, F.F., 2008. Observations and interpretation of fundamental mode Rayleigh wavefields recorded by the Transportable Array (USArray), *J. geophys. Res.,* **113,** B10311, doi:10.1029/2007JB005556.

Pollitz, F.F. & Snoke J.A., 2010, Rayleigh-wave phase-velocity maps and three-dimensional shear velocity structure of the western US from local non-plane surface wave tomography, *Geophys. J. Int.,* **180,** 1153–1169.

Rasmussen, J. & Humphreys, E., 1988. Tomographic image of the Juan de Fuca plate beneath Washington and western Oregon using teleseismic *P*-wave travel times, *Geophys. Res. Lett.,* **15,** 1417–1420, doi:10.1029/GL015i012p01417.

Ribe, N.M. & Christensen, U.R., 1994. Three-dimensional modeling of plume-lithosphere interaction, *J. geophys. Res.,* **99,** 669–682.

Riter, J.C.A. & Smith, D., 1996. Xenolith constraints on the thermal history of the mantle below the Colorado Plateau, *Geology,* **24,** 267–270.

Roth, J.B., Fouch, M.J., James, D.E. & Carlson, R.W., 2008. Three-dimensional seismic velocity structure of the northwestern United States, *Geophys. Res. Lett.,* **35,** L15304, doi:10.1029/2008GL034669.

Roy, M., Jordan, T.H. & Pederson, J., 2009. Colorado Plateau magmatism and uplift by warming of heterogeneous lithosphere, *Nature,* **459,** 978–982, doi:10.1038/nature08052.

Saleeby, J., 2003, Segmentation of the Laramide slab: evidence from the southern Sierra Nevada region, *Geol. Soc. Am. Bull.,* **115,** 655–668, doi: 10.1130/0016-7606(2003)115<0655:SOTLSF>2.0.CO;2.

Schmandt, B. & Humphreys, E., 2010. Complex subduction and small-scale convection revealed by body-wave tomography of the western United States upper mantle, *Earth planet. Sci. Lett.,* **297,** 435–445, doi:10.1016/j.epsl.2010.06.047

Schmandt, B. & Humphreys, E., 2011. Seismically imaged relict slab from the 55 Ma Siletzia accretion to northwest United States, *Geology,* **39,** 175–178, doi:10.1130/G31558.1.

Sigloch, K., McQuarrie, N. & Nolet, G., 2008. Two-stage subduction history under North America inferred from multiple-frequency tomography, *Nature Geosci.,* **1,** 458–462.

Sine, C.R., Wilson, D., Gao, W., Grand, S.P., Aster, R., Ni, J. & Baldridge, W.S., 2008. Mantle structure beneath the western edge of the Colorado Plateau, *Geophys. Res. Lett.,* **35,** L10303, doi:10.1029/2008GL033391.

Smith, R.B. & Braile, L.W., 1994. The Yellowstone hotspot, *J. Volc. Geotherm. Res.,* **61,** 121–187.

Smith, R.B. *et al.*, 2009. Geodynamics of the Yellowstone hotspot and mantle plume: seismic and GPS imaging, kinematics, and mantle flow, *J. Volc. Geotherm. Res.,* **188,** 26–56.

Steinberger, B., Sutherland, R. & O'Connell, R.J., 2004. Prediction of Emperor-Hawaii seamount locations from a revised model of global plate motion and mantle flow, *Nature,* **430,** 167–173.

Tian, Y., Sigloch, K. & Nolet, G., 2009, Multiple-frequency SH-wave tomography of the western US upper mantle, *Geophys. J. Int.,* **178**(3), 1384–1402, doi:10.1111/j.1365-246X.2009.04225.x.

Tromp, J. & Dahlen, F. A. 1993. Variational principles for surface wave propagation on a laterally heterogeneous Earth –III: potential representation, *Geophys. J. Int.,* **112,** 195–209.

VanDecar, J.C. & Crosson, R.S., 1990. Determination of teleseismic relative phase arrival times using multi-channel cross-correlation and least squares, *Bull. seism. Soc. Am.,* **80,** 150–169.

Van Der Lee, S. & Nolet, G., 1997. Upper mantle velocity structure of North America, *J. geophys. Res.,* **102,** 22 815–22 838.

van Hunen, J., van den Berg, A.P. & Vlaar, N.J., 2002, On the role of subducting oceanic plateaus in the development of shallow flat subduction, *Tectonophysics,* **352,** 317–333.

van Wijk, J.W., Baldridge, W.S., van Hunen, J., Goes, S., Aster, R., Coblentz, D.D., Grand, S.P. & Ni, J., 2010. Small-scale convection at the edge of the Colorado Plateau: implications for topography, magmatism, and evolution of Proterozoic lithosphere, *Geology,* **38,** 611–614, doi:10.1130/G31031.1.

Waite, G.P., Smith, R.B. & Allen, R.M., 2006, VP and VS structure of the Yellowstone hot spot from teleseismic tomography: evidence for an upper mantle plume, *J. geophys. Res.,* **111,** B04303, doi:10.1029/2005JB003867.

Wessel, P. & Smith, W.H.F., 1998, New, improved version of the Generic Mapping Tools released, *EOS Trans. Am. goephys. Un.,* **79,** 579.

West, M., Gao, W. & Grand, S., 2004, A simple approach to the joint inversion of seismic body and surface waves applied to the southwest U.S., *Geophys. Res. Lett.,* **31,** L15615, doi:10.1029/2004GL020373.

West, J.D., Fouch, M.J., Roth, J.B. & Elkins-Tanton, L.T., 2009. Vertical mantle flow associated with a lithospheric drip beneath the Great Basin, *Nature Geosci.,* **2,** 439–444.

Wong, I.G. & Humphrey, J.R., 1989. Contemporary seismicity, faulting, and the state of stress in the Colorado Plateau, *Geol. Soc. Am. Bull.,* **101,** 1127–1146.

Yang, Y. & Forsyth, D. W., 2006. Rayleigh wave phase velocities, small-scale convection, and azimuthal anisotropy beneath southern California, *J. geophys. Res.*, **111,** doi:10.1029/2005JB004180.

Yang, Y. & Ritzwoller, M.H., 2008. Teleseismic surface wave tomography in the western US using the Transportable Array component of USArray, *Geophys. Res. Lett.,* **35,** L04308, doi:10.1029/2007GL032278.

Yuan, H.Y. & Dueker, K. 2005, Teleseismic P-wave tomogram of the Yellowstone plume, *Geophys. Res. Lett.,* **32,** L07304, doi:10.1029/2004FL022056.

Zandt, G., Gilbert, H., Owens, T.J., Ducea, M., Saleeby, J. & Jones, C.H., 2004. Active foundering of a continental arc root beneath the southern Sierra Nevada in California, *Nature,* **431,** 41–46.